The Astrophysical Journal, 1001:226 (18pp), 2026 April 20 https://doi.org/10.3847/1538-4357/ae4d1a

Stratification of the Active Galactic Nucleus–Driven Multiphase Outflows in the Dwarf Seyfert Galaxy NGC 4395

Payel Nandi[1,2], Luis Colina[3], Rogemar A. Riffel[3,4], Miguel Pereira Santaella[5], C. S. Stalin[2], D.J. Saikia[6,7], Javier Álvarez-Márquez[3], and Markus Kissler-Patig[8]

[1] Inter-University Centre for Astronomy and Astrophysics, IUCAA, Pune 411007, India; nandipayel05@gmail.com
[2] Indian Institute of Astrophysics, Block II, Koramangala, Bangalore, 560034, India
[3] Centro de Astrobiología (CAB), CSIC-INTA, Ctra. de Ajalvir km 4, Torrejón de Ardoz, E-28850, Madrid, Spain
[4] Departamento de Física, CCNE, Universidade Federal de Santa Maria, 97105-900, Santa Maria, RS, Brazil
[5] Instituto de Física Fundamental, CSIC, Calle Serrano 123, 28006 Madrid, Spain
[6] Fakultat für Physik, Universität Bielefeld, Postfach 100131, D-33501 Bielefeld, Germany
[7] Assam Don Bosco University, Guwahati 781017, Assam, India
[8] European Space Agency (ESA), European Space Astronomy Centre (ESAC), Camino Bajo del Castillo s/n, 28692, Villanueva de la Cañada, Madrid, Spain

Received 2026 January 15; revised 2026 February 6; accepted 2026 February 7; published 2026 April 17

Abstract

We present a multiwavelength study of nuclear outflows in the nearby dwarf Seyfert galaxy NGC 4395, which hosts an intermediate-mass black hole. Using JWST/NIRSpec and MIRI integral-field-unit spectroscopy (1.66–28.6 μm), together with Atacama Large Millimeter/submillimeter Array (ALMA) and Gemini/GMOS data, we probe the ionized and molecular gas on parsec scales. The JWST nuclear spectra reveal 134 emission lines, including H I, He, numerous fine-structure lines, H_2 rotational/rovibrational transitions, and several polycyclic aromatic hydrocarbon bands. Modelling of the H_2 rotational lines reveals three warm/hot molecular components ($T \approx 580$, 1480, and 2900 K), along with a cold (< 50 K) phase traced by ALMA CO(2–1). Outflow signatures are detected in cold and warm/hot molecular gas, in H I, and in 36 fine-structure lines spanning ionization potentials of 7.6–300 eV. Ionized outflow velocities range from 127 to 716 km s^{-1}, with blueshifted and redshifted components consistent with a stratified biconical geometry. The cold molecular gas shows a mass outflow rate nearly 1–2 orders of magnitude larger than that of the warm/hot molecular and ionized phases. The kinetic coupling efficiency is 0.003%–0.12% for the coronal-line gas and 0.4%–1.4% for the H I outflow, indicating that only the low-ionization gas significantly impacts the surrounding ISM. Outflow velocity and the fraction of flux in the outflowing component increase with ionization potential, implying that the most highly ionized gas originates closest to the active galactic nucleus and is most efficiently accelerated.

Unified Astronomy Thesaurus concepts: Active galactic nuclei (16); Infrared spectroscopy (2285); Hot ionized medium (752); Molecular spectroscopy (2095); Molecular gas (1073)

Materials only available in the online version of record: data behind figure

1. Introduction

Active galactic nuclei (AGN) exert a significant influence on the formation and evolution of galaxies through powerful feedback mechanisms. These processes, driven either by radiation pressure or mechanical outflows such as radio jets, can regulate star formation, heat the interstellar medium (ISM), and redistribute gas across a wide range of spatial scales, from the inner few parsecs to kiloparsec-sized galactic structures (A. C. Fabian 2012; A. King & K. Pounds 2015; C. M. Harrison et al. 2018; S. Veilleux et al. 2020; P. Nandi et al. 2023a, 2023b, 2024; L. Hermosa Muñoz et al. 2024; P. Nandi & C. Subramonian Stalin 2024; L. Zhang et al. 2024).

AGN outflows are inherently multiphase, observed in ionized, neutral, and molecular gas, each tracing different regions and physical conditions of the ISM (R. A. Riffel et al. 2023; R. Su et al. 2023). These outflows span a wide velocity and spatial range, from ultrafast X-ray winds near the accretion disk (F. Tombesi et al. 2010) to extended molecular and ionized gas flows observed at kiloparsec scales (C. M. Harrison et al. 2014; T. Izumi et al. 2023).

Ultrafast outflows (UFOs), often detected in X-ray spectra through blueshifted absorption of Fe XXV or Fe XXVI, exhibit velocities $\gtrsim$10,000 km s^{-1} and are thought to originate within a few hundred gravitational radii from the central black hole (F. Tombesi et al. 2010). Intermediate UV absorbing outflows observed with Hubble Space Telescope show blueshifted resonance lines (e.g., C IV, O VI) with velocities of up to $\leqslant$3000–4000 km s^{-1}, tracing photoionized winds that bridge the gap between ultrafast X-ray winds and the slower warm ionized gas phases in many Seyferts and quasars (D. M. Crenshaw et al. 2004; N. Arav et al. 2015; M. Mizumoto et al. 2021). Warm ionized gas, traced through optical and near-infrared forbidden lines such as [O III]5007 or high-ionization coronal lines like [Fe VII] and [Ne V], exhibits typical velocities in the range of 500–2000 km s^{-1} and can extend to several kiloparsecs (A. Rodríguez-Ardila et al. 2002; F. Müller-Sánchez et al. 2011; A. Rodríguez-Ardila et al. 2025).

In contrast, molecular outflows trace the cooler gas reservoirs and are observed via CO, OH, or H_2 emission or absorption, including both the cold ($T < 100$ K) and warm/hot ($T \sim 100$–3000 K) phases. While these outflows are typically slower (a few hundred to ~1000 km s^{-1}), they often carry significant mass and momentum and are directly linked to the suppression or triggering of star formation (K. M. Dasyra & F. Combes 2011; C. Cicone et al. 2014; B. H. C. Emonts et al. 2014, 2017; F. Fiore et al. 2017; M. Pereira-Santaella et al. 2018, 2020; J. H. Costa-Souza et al. 2024; J. H. Leftley et al. 2024). Additionally, outflows in neutral atomic gas are seen in H I 21 cm absorption or optical Na I D lines, offering further insights into AGN-driven feedback processes on different scales (H. B. Krug et al. 2010; S. Cazzoli et al. 2016; R. Morganti & T. Oosterloo 2018; D. S. N. Rupke et al. 2021; R. L. Davies et al. 2024).

High-ionization coronal lines, such as [Ne V], [Fe VII], and [Mg VIII], offer a unique probe of the innermost energetic regions of the AGN, believed to reside between the classical narrow-line region (NLR) and the broad-line region (BLR; J. W. Ferguson et al. 1997; J. Álvarez-Márquez et al. 2023), where gas may be predominantly shock-heated or photoionized by the AGN continuum. However, such lines remain less commonly studied in outflow diagnostics compared to low-ionization species (A. Rodríguez-Ardila et al. 2002; F. Müller-Sánchez et al. 2011; M. A. Fonseca-Faria et al. 2023; M. Pereira-Santaella et al. 2024; A. Rodríguez-Ardila et al. 2025).

Disentangling the excitation mechanisms and kinematic signatures of these different gas phases is essential for understanding how AGN feedback regulates galaxy growth. Molecular gas, in particular, plays a critical role since it fuels star formation and can be strongly influenced by AGN activity. A holistic, multiphase view is thus key to capturing the full extent and impact of AGN feedback (F. Fiore et al. 2017; R. A. Riffel 2021). While some studies have examined multiphase outflows, most of them have focused on massive galaxies hosting luminous quasars (D. S. N. Rupke & S. Veilleux 2013) or Seyfert nuclei, such as in Cygnus A, NGC 424 (R. A. Riffel 2021; C. Marconcini et al. 2025); there is increasing interest in exploring feedback in low-mass galaxies hosting intermediate-mass black holes (IMBHs; $M_{\rm BH} \sim 10^4$–$10^6\,M_\odot$). These systems are crucial for understanding early black hole seed formation, low-mass end coevolution, and the effectiveness of AGN feedback in shallow gravitational potentials (A. E. Reines & M. Volonteri 2015; S. J. Penny et al. 2018; J. E. Greene et al. 2020). However, observational studies of such systems remain sparse, primarily due to their lower luminosities and compact sizes, which challenge both spatial and spectral resolution.

NGC 4395, located at 4.3 Mpc (F. Thim et al. 2004), is one of the best studied dwarf AGN with an IMBH of mass $\sim 10^5\,M_\odot$ (B. M. Peterson et al. 2005; A. V. Filippenko & L. C. Ho 2003; M. den Brok et al. 2015; S. Pandey et al. 2024). Despite its low bolometric luminosity ($L_{\rm bol} \sim 10^{41}$ erg s^{-1}), NGC 4395 shows pronounced nuclear activity, hosting hot ionized outflows traced by X-ray and UV absorbers (D. M. Crenshaw et al. 2004; D. M. Crenshaw & S. B. Kraemer 2012), as well as warm ionized outflows traced by optical [O III], which may be driven by a compact radio jet (P. Nandi et al. 2023b). Additionally, evidence for both negative and positive feedback modes has been reported on subkiloparsec scales (P. Nandi et al. 2023a, 2023b).

In this work, we analyzed JWST/NIRSpec and MIRI integral field unit (IFU) spectra, complemented by Atacama Large Millimeter/submillimeter Array (ALMA) and Gemini Multi-Object Spectrograph (GMOS) observations, to carry out a comprehensive study of nuclear outflows in NGC 4395 across the near- and mid-infrared, molecular, and optical bands. This paper is structured as follows: Section 2 describes the observations and data reduction; Section 3 presents the main results, including emission-line diagnostics and kinematic profiles; Section 4 discusses the multiphase nature of the outflows, their dependence on ionization potential (IP; the energy required to produce the ionization stage responsible for the observed line), and the implications for AGN feedback in dwarf galaxies; and Section 5 summarizes the key conclusions. Throughout this paper, we adopt a distance of 4.3 Mpc to NGC 4395 (F. Thim et al. 2004), corresponding to a scale of 21 pc arcsec^{-1}.

2. Observations and Data Reduction and Analysis

2.1. JWST

We utilized archival IFU observations from the JWST obtained under Program ID 2016 (PI: Anil C. Seth; K. Goold et al. 2026; doi:10.17909/b8qa-jn82). These observations were conducted using JWST's two primary spectroscopic instruments: NIRSpec (P. Jakobsen et al. 2022) and MIRI (G. H. Rieke et al. 2015; G. S. Wright et al. 2015; G. S. Wright et al. 2023).

For the NIRSpec IFU observations, we used data acquired in high-resolution mode with the `G235H` and `G395H` gratings, coupled with the `F170LP` and `F290LP` filter configurations, respectively. These configurations collectively cover the 1.66–5.2 μm wavelength range at a spectral resolving power $R \approx 1000$–5000 (T. Böker et al. 2023). These observations were performed using a four-point dither strategy, enhancing spatial coverage and minimizing residual detector-related artifacts such as bad pixels and interpixel capacitance.

For MIRI, the IFU data span all four spectral channels (Ch1–Ch4), each subdivided into three spectral subbands: short, medium, and long, resulting in a total of 12 spectral segments. These observations were also performed using a four-point dither strategy. MIRI's IFU mode provides moderate spectral resolution ($R \approx$ 1500–3500) across the 4.9–28.6 μm wavelength range (A. Labiano et al. 2021; I. Argyriou et al. 2023; O. C. Jones et al. 2023).

The raw uncalibrated data were downloaded from the Barbara A. Mikulski Archive for Space Telescopes portal and then reduced using the official `jwst` calibration pipeline (version 1.17.2), along with CRDS reference files from CRDS context `1322.pmap` (P. Greenfield & T. Miller 2016). For both instruments, we employed `Stage 1` and `Stage 2` of the pipeline, which perform detector-level corrections and spectrophotometric calibrations.

For MIRI, we implemented an additional step to identify and mask warm pixels, using background exposures from `Stage 2` products to generate pixel masks. These were applied to the corresponding science frames before proceeding to `Stage 3`, where the final three-dimensional data cubes were constructed using the `Drizzle` algorithm (D. R. Law et al. 2023). During `Stage 3`, we enabled master background subtraction to remove residual thermal and instrumental background contributions, benefiting from dedicated background exposures available for these observations.

In the case of NIRSpec, we similarly employed `Stage 1` and `Stage 2` of the pipeline. Additionally, to address the presence of $1/f$ noise, we applied the `NSClean` algorithm during `Stage 2`. As the NIRSpec program did not include separate background observations, no background subtraction was performed for these data. Then, we ran `Stage 3` of the pipeline to combine all the exposures and construct the cube using the `Drizzle` method. We also rescaled our pixel to 0.″05.

From the fully calibrated IFU data cubes, we extracted the nuclear spectra of the central AGN using a circular aperture with a radius of 0.″5 for the NIRSpec gratings and MIRI Channels 1 and 2. Owing to the increasing degradation of the point-spread function (PSF) at longer wavelengths, a larger aperture of 1″ was adopted for MIRI Channels 3 and 4 to account for the extended PSF wings. To ensure accurate flux calibration within each aperture, we performed wavelength-dependent PSF simulations using the `Space Telescope PSF` package (M. D. Perrin et al. 2012; M. D. Perrin et al. 2014), which incorporates instrumental effects such as geometric distortion and detector charge transfer inefficiencies. The extracted spectra were corrected for aperture flux losses using the corresponding PSF models, enabling reliable recovery of the intrinsic AGN flux across the full near- to mid-infrared spectral range.

A relative offset of 2×10^{-18} erg s^{-1} cm^{-2} was identified between all channels and Channel 4. In addition, Channel 4C exhibited an extra deviation of 5×10^{-18} erg s^{-1} cm^{-2} relative to Channels 4A and 4B. These discrepancies were corrected by applying vertical shifts: Channels 4A and 4B were shifted downward by 2×10^{-18} erg s^{-1} cm^{-2}, while Channel 4C was shifted upward by 5×10^{-18} erg s^{-1} cm^{-2}.

2.2. ALMA

To probe the cold molecular gas component of the outflows, we utilized high-spectral-resolution observations from ALMA. In particular, we analyzed archival `Band 6` observations obtained with the 12 m array, under project ID `2017.1.00572.S` (PI: Timothy Davis). We utilized the pipeline-calibrated and primary beam-corrected data cube available from the ALMA Science Archive, which had been processed using `CASA` version `5.4.0-68`. The FWHM of the synthesized beam is 1.″99 × 1.″29. The spectral resolution is uniformly high across the band, with channel spacing of 0.63–0.64 km s^{-1}, enabling precise characterization of narrow molecular line components. Spectral extraction was performed using an aperture matched to the beam size, centered on the flux-weighted centroid of the emission as derived from the velocity-collapsed line map, which is ∼0.″9 far from the center of the nucleus toward northward west direction as reported in P. Nandi et al. (2023b).

2.3. GMOS

In addition to millimeter and infrared observations, we incorporated optical IFU spectroscopy obtained with the GMOS on the Gemini-North telescope to use optical coronal lines [Fe VII] for our density-temperature analysis. These data were obtained as part of program GN-2015A-DD-6 (PI: Rachel Mason), and cover the central region of the galaxy with a spectral range of 4450–7347 Å. From the final reduced GMOS data cube (see C. Brum et al. 2019 and P. Nandi et al. 2023b for a detailed description of the observations and data reduction procedures), we extracted the integrated optical spectrum within a circular aperture of radius 0.″5 centered on the nucleus, matching the apertures used for the infrared observations.

3. Results

3.1. Identification of Lines and their Characteristics

We extracted nuclear spectra from the JWST/NIRSpec and MIRI instruments, covering the full spectral range from 1.66 to 28.6 μm.

To systematically identify and characterize the spectral features in the extracted spectra, we utilized the Atomic Line List[9] and cross-referenced them with values reported in the literature. In total, we identified 134 distinct emission lines and polycyclic aromatic hydrocarbon (PAH) features across the combined NIRSpec and MIRI wavelength range. Of these, 91 were detected in the NIRSpec spectra and 50 in the MIRI spectra, with seven lines appearing twice due to overlapping wavelength coverage between the NIRSpec G235H, NIRSpec G395H gratings and the MIRI subbands. The nuclear spectrum, with several of the prominent emission lines marked, is presented in Figure 1.

Following the identification of individual emission lines, we employed a multi-Gaussian fitting procedure to derive integrated fluxes and kinematic properties for each spectral feature. We first attempted a single-Gaussian fit for the line, combined with a first-order polynomial for the local continuum, and inspected the residuals. If the residuals within the line region exceeded those in the continuum by more than a factor of 2, we added a second Gaussian component while retaining the polynomial continuum (see P. Nandi et al. 2025 for details). In practice, we found that a maximum of two Gaussians was sufficient to model all lines except three strong H I recombination lines. The full list of detected features, along with their measured fluxes and wavelengths, is provided in Table C1. This approach ensured a consistent treatment of blended or asymmetric profiles and enabled us to separate narrow and broad components in cases where the line shapes indicated the presence of outflowing gas.

During the line-fitting analysis, we noted that several emission lines in the MIRI spectra, especially those arising in Channels 3 and 4, exhibited FWHM values that were narrower than the nominal instrumental resolution as determined from in-flight performance measurements (I. Argyriou et al. 2023). To assess the reliability and physical plausibility of these narrow features, we cross-validated our FWHM measurements with recent studies of high-resolution MIRI spectra in circumstellar disk systems (K. M. Pontoppidan et al. 2024; A. Banzatti et al. 2025). These works reported similarly narrow emission lines, suggesting that, when instrumental resolution is properly accounted for and a conservative uncertainty budget (10%) is included, such measurements remain credible. Our comparison, illustrated in Figure A1, shows good agreement with these prior results and supports the interpretation that narrow, unresolved, or marginally resolved lines can persist in AGN environments, particularly in low-luminosity systems where turbulent and bulk velocities may be modest.

Furthermore, we observed that the emission lines detected in the NIRSpec spectra also displayed FWHM values that were systematically smaller than those expected from ground-based

---

[9] https://linelist.pa.uky.edu/atomic/

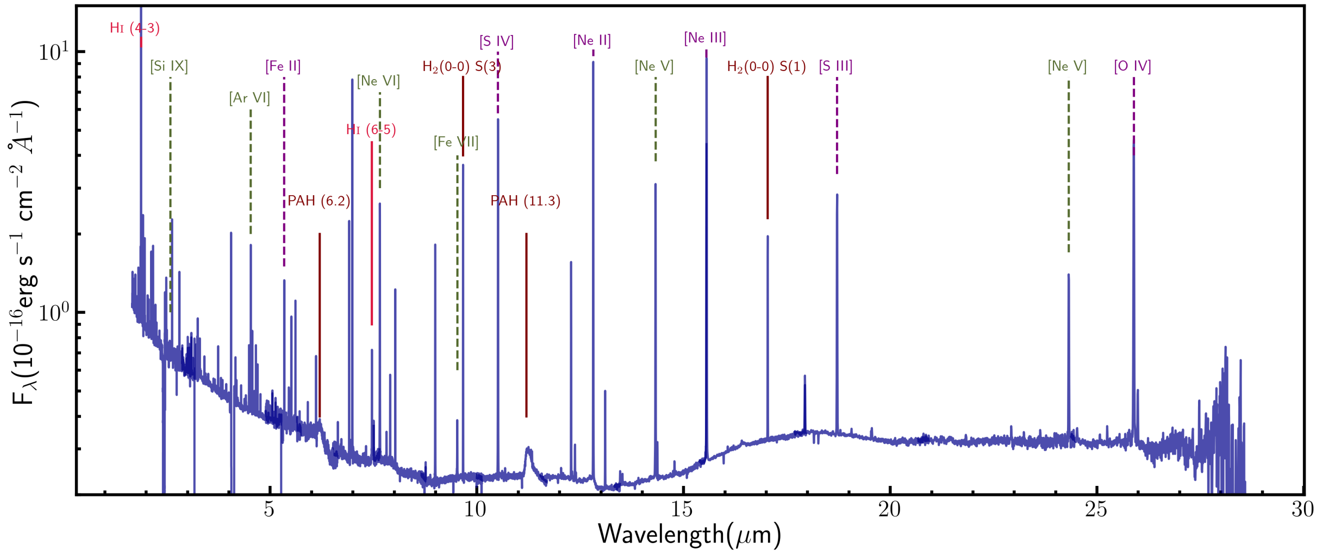

Figure 1. Aperture-corrected nuclear spectrum of NGC 4395, extracted from the central region, spans the rest-frame wavelength range 1.66–28.6 μm, combining observations from JWST/NIRSpec and MIRI Channels 1–4. Some of the prominent emission lines are indicated along the spectrum. Molecular features, including PAH and H_2 lines, together with HI recombination lines, are shown by solid lines, while ionized gas lines are denoted by dashed lines. Low-ionization species (e.g., [Fe II], [Ne II], [S III], [O IV]) are marked in purple, whereas high-ionization lines are indicated in dark green.

(The data used to create this figure are available in the online article.)

calibration observations. However, when compared against reported uncertainties in ground-based instrumental resolution, our measurements remained within the 30% error range cited in the literature. This consistency, demonstrated in Figure A1, provides additional confidence in the robustness of our line-fitting methodology and supports the physical interpretation of the observed line widths.

Importantly, for all lines in both MIRI and NIRSpec, in which an outflow component was identified, the FWHM of that component exceeded the instrumental resolution, and we corrected for instrumental broadening in all outflow-related measurements.

3.1.1. Hydrogen Recombination Lines

We identified multiple hydrogen recombination (H I) lines (a total of 24 lines) across the Paschen (Pa), Brackett (Br), Pfund (Pf), and Humphreys (Hu) series in the near- and mid-infrared spectral range, which trace photoionized gas associated with both AGN activity and circumnuclear star formation. Among the Paschen lines, only the Paα transition was detected within the wavelength coverage of our observations; it is the strongest H I line.

In the Br series, we detected six transitions, ranging from Brβ to Brη. The Brα line, which falls in the gap between detectors in the NIRSpec/G235H grating, was not covered and thus could not be measured. The Pf series is well-sampled, with eight lines detected from Pfα up to Pf(13–5), while in the Hu series, we identified seven lines, extending from Huα to Huη.

In addition to these classical series, we also detected two higher-order hydrogen recombination transitions. These include one line from levels with a lower principal quantum number $n = 7$, specifically H I (11–7) with a signal-to-noise ratio (SNR) of 3.77. We also report the detection of a line at 12.387 μm corresponding to a transition between the $n = 11$ and $n = 8$ energy levels, with a SNR of 3.07.

Most of the H I lines (except for weak transitions such as Pf(13–5), Hu(13–6), H I(11–7), and H I(11–8)) are best fitted with two Gaussian components, including a blueshifted broad component. For the stronger H I lines, such as Paα, Brβ, and Brγ, where the SNR exceeds 40, we were able to clearly disentangle the contribution from the very broad (FWHM $>$ 1300 km s^{-1}) BLR component. These lines were modeled with three Gaussian components: one representing the NLR, another for the BLR (sharing the same systemic velocity as the NLR), and a third blueshifted component accounting for the outflow emission, following the approach of P. Nandi et al. (2023b). We then only considered the NLR and the outflow component for our further analysis.

3.1.2. Helium Lines

We identified eight helium emission lines in the NIRSpec spectrum, including six He II recombination lines and two neutral He I recombination transitions. Most of these lines were well modeled with a single-Gaussian component. Only He I 1.869 μm and He II 4.7635 μm required two components; however, the BLR component could not be reliably resolved due to the modest SNR (SNR $<$ 40) of these features. These helium lines originate in highly ionized gas and provide important diagnostics for probing the hardness of the ionizing radiation field.

3.1.3. Fine-structure Atomic Lines

We detected a rich set of forbidden emission lines (total 61 lines) from a wide array of ionized species, including heavy elements such as [O IV], [Ne II], [Ne III], [Ne V], [Ne VI], [Ni II], [Na III], [Na VII], [Mg V], [Mg VII], [Mg VIII], [Si IX], [S III], [S IV], [Ar II], [Ar III], [Ar V], [Ar VI], [Ca IV], [Cl V], [K III], [Fe II], [Fe III], [Fe VII], [Co II]. These lines span a broad range of IP, from ∼7.6 eV (e.g., [Ni II]) to ∼303 eV (e.g., [Si IX]), enabling a comprehensive investigation of the ionized gas conditions in the nuclear region.

Low- and intermediate-ionization lines (e.g., [S III], [Ne II], [Fe II]) trace photoionized regions associated with the extended NLR, while high-ionization lines (e.g., [Ne V], [Fe VII], [Si IX]) are unambiguous tracers of AGN activity and can also be excited by fast ($v \gtrsim 200$ km s^{-1}) radiative shocks (e.g., M. G. Allen et al. 2008; R. S. Sutherland & M. A. Dopita 2017).

3.1.4. Molecular Hydrogen (H_2) Lines

A comprehensive set of 41 molecular hydrogen (H_2) emission lines, including both rotational and rovibrational transitions, was detected using the NIRSpec and MIRI data between 1.75 and 17.04 μm. These lines provide valuable insights into the properties of warm and hot molecular gas in the nuclear region.

We identified 15 pure rotational lines from the 0–0 S-branch, ranging from H_2 S(1) at 17.035 μm to H_2 S(15) at 3.6263 μm. Two lines from the 1–1 S-branch, H_2 S(9) and H_2 S(10), were also detected; however, H_2(1–1) S(10) is blended with the strong H I recombination line Pfβ, making its detection uncertain.

From the $v = 1$–0 rovibrational band, we detected sixteen lines: eight in the S-branch (H_2 S(0) to S(7)), five in the O-branch, and three in the Q-branch (H_2 Q(5), Q(6), and Q(7)). The Q(1) to Q(4) lines fall in a detector gap of the NIRSpec/G235H grating and could not be observed. The five detected O-branch transitions range from H_2(1–0) O(3) at 2.8025 μm to H_2(1–0) O(7) at 3.8074 μm. H_2(1–0) O(2), which lies at 2.6269 μm, is blended with Brβ, complicating its detection.

We also detected higher-excitation rovibrational lines from the $v = 2$–1 band, including two S-branch lines (H_2 S(0) and S(1)) and four O-branch lines (H_2 O(3) to O(6)). Additionally, two O-branch transitions from the $v = 3$–2 band, H_2 O(3) and O(5), were identified.

Some of the H_2 emission lines are narrow, with widths comparable to the instrumental resolution, indicating that the emitting gas is kinematically quiescent. The excitation of this warm and hot molecular gas traced through these pure rotational and rovibrational transitions, with temperatures ranging from a few hundred to a few thousand Kelvins, is likely driven by a combination of ultraviolet fluorescence, X-ray heating, and shock mechanisms commonly associated with AGN activity (H. Mouri 1994).

3.1.5. PAH Features

In addition to the emission lines shown in Figure 1, we clearly detect prominent PAH features at 3.3, 6.2, and 11.3 μm. We also identify a broad hump between 15 and 20 μm, corresponding to the PAH plateau in this wavelength range (A. Tappe et al. 2006). This feature likely arises from the blending of several weak PAH bands (e.g., 15.8, 16.4, 17.4, and 17.8 μm) emitted by large neutral or ionized PAH molecules, producing a smooth continuum-like "hump" (e.g., A. Tappe et al. 2006; J. D. T. Smith et al. 2007; C. Boersma et al. 2010).

A possible additional contribution may come from thermal emission by warm dust grains in the torus or the circumnuclear ISM. Graphite and silicate grains with temperatures of 150–300 K can emit strongly in this spectral region, producing a broad mid-infrared continuum bump (e.g., M. Contini et al. 2004; R. Mor et al. 2009; E. Hatziminaoglou et al. 2015). In such cases, the 10 μm silicate feature often appears in emission (as seen in several type 1, unobscured AGN), with its long-wavelength tail extending toward ~20 μm (I. García-Bernete et al. 2017). However, in our spectrum of NGC 4395, we do not detect silicate emission at 10 μm, while a strong 11.3 μm PAH feature is clearly present. This suggests that the observed 15–20 μm bump predominantly originates from the PAH plateau rather than from thermal dust emission.

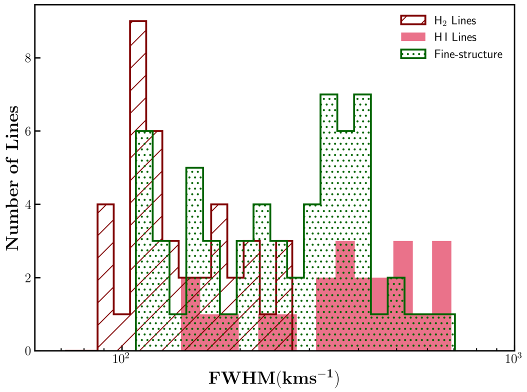

Figure 2. Distribution of the observed FWHM values (uncorrected for instrumental resolution) for the different gas phases: H_2, H I, and fine-structure lines.

These broad PAH bands are attributed to the vibrational modes of large carbonaceous molecules that can survive in the harsh radiation field of the AGN, indicating the presence of resilient PAH populations in the circumnuclear environment (e.g., E. L. Lambrides et al. 2019; I. García-Bernete et al. 2024; D. Rigopoulou et al. 2024).

3.2. Emission-line Widths and Kinematics

The distribution of the observed emission-line widths (FWHM) is presented in Figure 2 for the molecular H_2, H I, and fine-structure lines. For the H I lines, we adopted the combined FWHM of the narrow and broad components for all transitions, and the sum of the narrow and broad outflow components for the three lines where a distinct BLR contribution could be fitted, as discussed in Section 3.1.1. The H I lines exhibit significant broadening, with FWHM values ranging from 141 to 690 km s^{-1} and a median of 422 km s^{-1}. The wide spread in widths likely arises because some higher-order transitions appear narrower, possibly due to the absence of a detectable broad component from outflow and also BLR, which may in turn result from lower SNR.

In contrast, fine-structure lines that follow highly ionized species also exhibit a wide range of kinematic widths, with FWHM values ranging from 108 to 705 km s^{-1} and a median of 286 km s^{-1}. These kinematic features are consistent with earlier studies of fine-structure lines in AGN, which show line broadening as a signature of outflowing ionized gas and stratified emission regions (E. L. Escott et al. 2025; P. Nandi et al. 2025).

Molecular hydrogen (H_2) emission lines exhibit the narrowest kinematic signatures among all detected species. The measured FWHM values span from 72 to 272 km s^{-1}, with a median of 126 km s^{-1}. However, three rovibrational H_2 (1–0) transitions—namely, S(5), S(6), and S(7)—display tentative broad components with FWHM exceeding 400 km s^{-1}. Given the low SNRs and large uncertainties associated with these features, we exclude

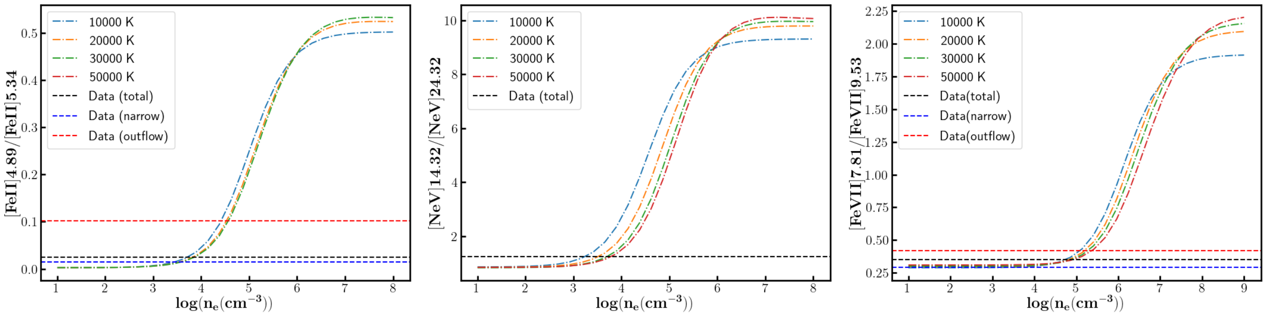

Figure 3. Variation in different line ratios with density for different particular temperatures, which represent different curves in each plot and are denoted by individual legends in each plot. The horizontal lines in each plot represent the observed line ratio.

Table 1
Electron Density Measured from Different Tracers at Different T_e

Lines	n_e (10,000 K) (10^4 cm^{-3})	n_e (20,000 K) (10^4 cm^{-3})	n_e (30,000 K) (10^4 cm^{-3})	n_e (50,000 K) (10^4 cm^{-3})
[Fe II]4.89/[Fe II]5.34 (total)	0.50 ± 0.04	0.65 ± 0.06	0.71 ± 0.06	0.82 ± 0.06
[Fe II]4.89/[Fe II]5.34 (narrow)	0.27 ± 0.02	0.34 ± 0.03	0.37 ± 0.04	0.43 ± 0.04
[Fe II]4.89/[Fe II]5.34 (outflow)	2.58 ± 0.22	3.34 ± 0.31	3.65 ± 0.34	4.25 ± 0.04
[Ne V]8.91/[Ne V]24.3 (total)	0.17 ± 0.04	0.33 ± 0.09	0.51 ± 0.10	0.61 ± 0.16
[Fe VII]7.81/[FeVII]9.53 (total)	5.20 ± 2.25	6.36 ± 3.04	7.39 ± 3.74	7.88 ± 4.87
[Fe VII]7.81/[FeVII]9.53 (narrow)[a]	…	…	…	…
[Fe VII]7.81/[FeVII]9.53 (outflow)	12.19 ± 3.05	15.65 ± 4.11	18.61 ± 5.17	23.64 ± 6.76

Note.
[a] This ratio lies below the theoretical limit, as shown in the right panel of Figure 3.

them from our statistical analysis to avoid biasing the FWHM distribution. The narrow widths of the lower-level H_2 lines are consistent with previous results from Gemini/NIFS observations of this system (C. Brum et al. 2019). This range of line widths likely reflects combination excitation through UV fluorescence or thermal processes within rotating molecular structures, such as disks or compact tori or shocks (A. Sternberg 1989a; R. I. Davies et al. 2005).

3.3. Electron Density and Temperature Diagnostics

We determined the electron density (n_e) and electron temperature (T_e) in the nuclear region of NGC 4395 through a detailed analysis of multiple low- and high-ionization emission lines, utilizing the `PyNeb` package (V. Luridiana et al. 2015). A variety of diagnostic line ratios were selected to sample a wide range of physical conditions that are insensitive to either T_e or n_e, allowing for reliable and independent constraints on both parameters. We corrected all lines for extinction effect using K. D. Gordon et al. (2023) reddening law and adopting $A_V = 0.96$ (C. Brum et al. 2019; P. Nandi et al. 2023b).

To characterize the low-ionization phase of the ionized gas, we analyzed several prominent [Fe II] emission-line ratios. Among these, the [Fe II]4.89/[Fe II]5.34 ratio is particularly effective, as it shows strong sensitivity to electron densities in the range 10^3–10^6 cm^{-3}, while exhibiting only a weak dependence on T_e (see Figure 3), consistent with the findings of M. Pereira-Santaella et al. (2022). We evaluated this diagnostic across representative temperatures of 10,000, 20,000, 30,000, and 50,000 K. From the observed [Fe II] 4.89/5.34 ratio, we derived electron densities in the range (0.50–0.82) × 10^4 cm^{-3} (n_e for individual components are given in Table 1).

These values are significantly higher than those inferred from optical [S II] doublet diagnostics in P. Nandi et al. (2023b), which probe more extended, lower-density gas. Similar trends have been observed in other AGN (e.g., R. A. Riffel 2021), highlighting that [Fe II] emission lines are more responsive to shock-excited gas and originate from regions closer to the central engine, where densities are typically higher.

When separating the line emission into narrow and broad kinematic components, we found that the narrow components yield electron densities of (0.27–0.43) × 10^4 cm^{-3}, in better agreement with values derived from [S II] diagnostics (P. Nandi et al. 2023b). In contrast, the broad components exhibit considerably higher densities, ranging from (2.58–4.25) × 10^4 cm^{-3}, indicating that the high-velocity outflowing gas is associated with denser regions likely located closer to the nucleus.

To probe the highly ionized gas component, we employed diagnostic transitions of [Ne V] and [Fe VII]. For [Ne V], we detected emission lines at 14.32 and 24.32 μm, enabling the use of the [Ne V]14.32/[Ne V]24.32 line ratio—a commonly adopted tracer of electron density in high-ionization regions (S. Tommasin et al. 2008; M. Pereira-Santaella et al. 2010; K. M. Dasyra et al. 2024). Based on the observed fluxes, we derived electron densities in the range of (0.17–0.61) × 10^4 cm^{-3} over the adopted temperature grid. In particular, due to the reduced sensitivity of the line, the limited spectral resolution, and the relatively low intensity of the [Ne V] 24.32 μm line, we were unable to resolve the outflow component. As a result, n_e estimates for individual kinematic components could not be determined in this case.

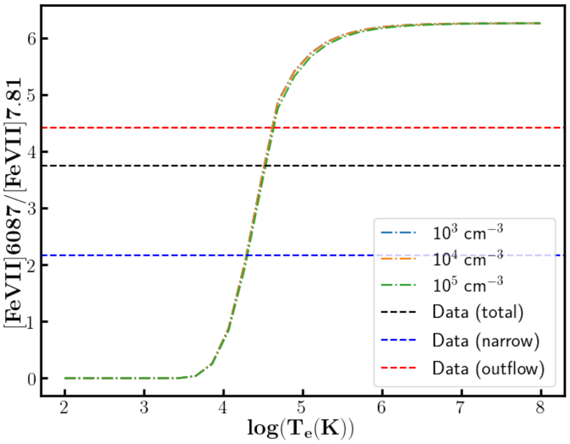

Figure 4. Variation in [Fe VII]λ6087 Å and [Fe VII]λ7.81 μm line ratio with electron temperature for different particular electron densities, which represent different curves in each plot and are denoted by individual legends in each plot. The horizontal line in the plot represents the observed line ratio.

We also investigated the physical conditions of the highly ionized gas phase using [Fe VII] transitions, with three prominent lines detected, two in the mid-infrared at 7.81 and 9.53 μm, and one in the optical at 6087 Å. Among the available diagnostics, the [Fe VII]7.81/[Fe VII]9.53 ratio was found to be the most robust tracer of electron density, due to its minimal sensitivity to T_e across a broad density range (10^4–10^8 cm^{-3}; see Figure B1). Using this ratio, we derived electron densities between (5.20–7.88) × 10^4 cm^{-3}. These values are approximately an order of magnitude higher than those inferred from [Ne V] diagnostics, despite both ions having comparable IPs (IP([Fe VII]) = 99.1, IP([Ne V]) = 97.1), suggesting [Fe VII] traces a denser, more compact ionized region closer to the nucleus.

While splitting into two components, the narrow component, associated with spatially extended emission, exhibited electron densities below 10^4 cm^{-3}. In contrast, the outflow component displayed substantially higher electron densities, in the range of $(12.19–23.64)\times10^4$ cm^{-3}. This trend matches that in [Fe II], though [Fe VII] line ratios indicate densities several times higher, supporting the view that the outflow arises from denser, more turbulent regions near the active nucleus.

Table 1 summarizes the density estimates derived from the [Fe II] 4.89/[Fe II] 5.34, [Ne V] 8.91/[Ne V] 24.3, and [Fe VII] 7.81/[Fe VII] 9.53 line ratios. A careful inspection of Figure 3 indicates that the observed ratios lie within the rising, density-sensitive portion of the diagnostic curves, with the exception of the narrow components, which approach the lower-density end. In contrast, the ratios associated with the outflow components occupy higher values, implying correspondingly higher electron densities.

To estimate the T_e of the ionized gas, we employed multiple [Fe VII] line ratios, focusing in particular on the [Fe VII] λ6087 Å and [Fe VII]λ7.81 μm ratio due to its high sensitivity to T_e and relatively weak dependence on electron density (n_e), as illustrated in Figure 4, compared to the other two combinations shown in Figure B2. We considered a range of plausible electron densities spanning 10^3–10^5 cm^{-3}, adopting representative values of 10^3, 10^4, and 10^5 cm^{-3}. The corresponding extinction-corrected temperature estimates for the integrated emission are T_e = 32,911 ± 3056 K, 33,168 ± 3072 K, and 34,429 ± 3159 K, respectively.

When decomposing the emission into distinct kinematic components, we found a notable contrast in temperature between the narrow and broad components. For the narrow component, the derived temperatures are T_e = 19,593 ± 1037 K, 19,709 ± 1035 K, and 20,300 ± 1071 K across the same density grid. In contrast, the broad component yields significantly elevated temperatures of T_e = 41,658 ± 5483 K, 41,780 ± 5681 K, and 43,392 ± 6571 K. This substantial temperature difference may reflect additional heating mechanisms such as fast shocks or enhanced photoionization in the broad-line-emitting region, likely linked to AGN-driven outflows (R. A. Riffel et al. 2021).

These [Fe VII]-based temperatures are considerably higher than those derived from classical low-ionization diagnostics, such as [O III] and [N II] line ratios, which typically yield $T_e \sim$ 15,000–18,000 K (P. Nandi et al. 2023b). This discrepancy underscores the multiphase nature of the ionized gas and highlights the importance of high-ionization tracers in probing the energetic environment of the AGN NLR.

These results reveal a clear stratification in both n_e and T_e across the ionized gas phases, with elevated values consistently associated with more highly ionized species and kinematically disturbed components. In particular, the [Fe VII] emission arises from regions of significantly higher density and temperature compared to those traced by lower-ionization lines, indicating its origin in more compact and energetically active zones (A. Rodríguez-Ardila et al. 2002, 2005). This observed stratification is in agreement with theoretical expectations for AGN NLRs shaped by a combination of photoionization, radiation pressure, and shock excitation (J. W. Ferguson et al. 1997; A. Rodríguez-Ardila & F. Cerqueira-Campos 2025).

3.4. Ionized Gas Mass Traced through H I Recombination Lines

We estimated the ionized gas mass ($M_{\rm ion}$) from the H I line luminosities using Equation A5 of M. Revalski et al. (2022). All lines were corrected for extinction following the K. D. Gordon et al. (2023) reddening law and adopting $A_V = 0.96$ (C. Brum et al. 2019; P. Nandi et al. 2023b). This method is generally applicable to any H I transition and is particularly effective when high-resolution optical or infrared spectra are available. The ionized mass is computed as:

$$M_{\rm ion} = \left(\frac{L_{\rm H\,I}}{\rm erg\ s^{-1}}\right)\left(\frac{\epsilon_{\rm H\,I}}{\rm erg\ cm^3\ s^{-1}}\right)^{-1}\left(\frac{m_p^{\rm eff}}{n_p^{\rm eff}}\right), \quad (1)$$

where $L_{\rm H\,I}$ is the luminosity of the H I recombination line, $\epsilon_{\rm H\,I}$ is the emissivity derived under Case B recombination, $m_p^{\rm eff}$ is the effective proton mass, and $n_p^{\rm eff}$ is the effective proton density. Given the presence of metals and helium in the ionized gas, we adopted correction factors to account for the total particle mass and charge contribution: $m_p^{\rm eff} = 1.4\ m_p$ and $n_p^{\rm eff} = 1.1\ n_e$, consistent with assumptions in prior works (e.g., M. Revalski et al. 2022).

We implemented this approach on the extinction-corrected fluxes of the near- and mid-infrared hydrogen recombination lines—Paα, Brγ, and Pfα. The corresponding emissivities ($\epsilon_{\rm H\,I}$) were calculated using the `PyNeb` package (V. Luridiana et al. 2015), assuming Case B recombination conditions as described in D. E. Osterbrock & G. J. Ferland (2006). We used an electron temperature of T_e = 16,000 K and an electron density of $n_e = 2000\ \mathrm{cm}^{-3}$ based on our previous estimate, and we derived ionized gas masses of (1269 ± 47) $M_\odot$ from Paα and (998 ± 96) $M_\odot$ from Brγ. The close agreement between these estimates reinforces the consistency of our methodology across transitions that probe different depths of the ionized medium.

3.5. Molecular Gas Excitation and Mass Estimation

We investigated the physical conditions of the molecular gas in the nuclear region of NGC 4395 using both mid-infrared pure rotational and near-infrared rovibrational H_2 emission lines. In the mid-infrared, a total of 15 pure rotational transitions, from S(1) to S(15), were detected, providing sensitive diagnostics of the warm molecular gas and its excitation mechanisms (A. Sternberg 1989b; R. I. Davies et al. 2005; L. E. Kristensen et al. 2023). All line fluxes were corrected for extinction following K. D. Gordon et al. (2023) and subsequently modeled using the Photo Dissociation Region (PDR) Toolbox (M. W. Pound & M. G. Wolfire 2011).

The excitation diagram constructed from the pure rotational lines (upper panel of Figure 5) is best described by a three-component temperature model, which provides a significantly improved fit compared to a two-component solution. The best-fit temperatures correspond to a warm component at 582 ± 1 K, a hot component at 1484 ± 6 K, and a very hot component at 2917 ± 169 K. Such a temperature stratification is consistent with shock heating associated with AGN-driven winds or local turbulence for the warm and hot components, while the very hot component likely traces a small fraction of highly excited H_2 produced by nonthermal excitation processes, such as UV or X-ray pumping (e.g., A. Rodríguez-Ardila et al. 2004; P. Ogle et al. 2010).

To independently assess the excitation mechanism inferred from the mid-infrared analysis, we further examined the near-infrared rovibrational H_2 emission using extinction-corrected line ratios. Following the approach of R. A. Riffel (2021), we constructed excitation diagrams involving diagnostic ratios such as H_2(2–1) S(1)/H_2(1–0) S(1) and H_2(1–0) S(2)/H_2(1–0) S(0), shown in the lower panel of Figure 5. These ratios are sensitive to deviations from local thermodynamic equilibrium and therefore provide a complementary probe of the excitation conditions. The observed line ratios are consistent with predominantly thermal excitation, in agreement with the temperature structure inferred from the pure rotational transitions.

The total line-of-sight molecular hydrogen column density derived from the PDR Toolbox model is

$$N(\mathrm{H_2})_{\mathrm{total}} = (1.20 \pm 0.07) \times 10^{20}\ \mathrm{cm}^{-2},$$

dominated by the warm component $(1.21 \pm 0.07) \times 10^{20}\ \mathrm{cm}^{-2}$. The hot component contributes $(7.11 \pm 0.43) \times 10^{17}\ \mathrm{cm}^{-2}$, and the very hot phase contributes $(2.90 \pm 0.98) \times 10^{16}\ \mathrm{cm}^{-2}$.

Using a mean molecular weight of $\mu = 2.8$, and estimating the mass via $M_{\mathrm{mol}} = \mu m_p N_{\mathrm{H_2}} A$, we derive a total molecular gas mass of

$$M_{\mathrm{mol}} = 936 \pm 52\ M_\odot.$$

The warm phase overwhelmingly dominates the mass budget (930 ± 52 $M_\odot$), while the hot (6 ± 0.3 $M_\odot$) and very hot (0.2 ± 0.07 $M_\odot$) components contribute less than 1%.

When we then further calculate the cold molecular gas mass traced through the CO(2–1) line in ALMA, we first derive the CO line luminosity using

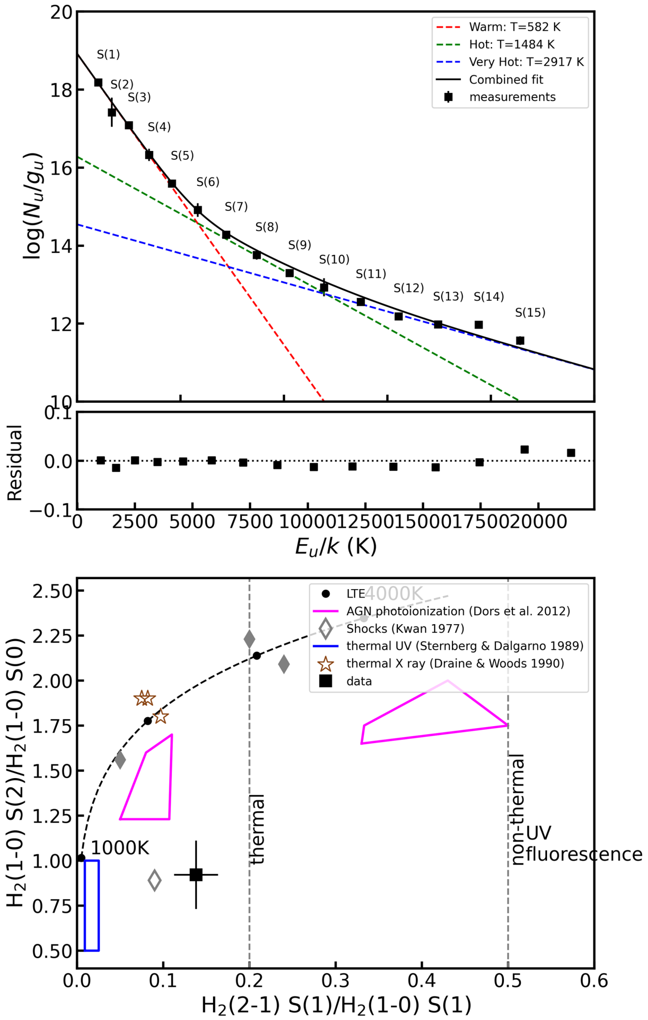

Figure 5. Upper panel: rotational excitation diagram of the pure molecular hydrogen emission lines. The solid lines indicate the best-fit models, while the points represent the observed data. The residual panels show the normalized residuals, defined as (data−model)/data. Lower panel: excitation diagram of the H_2 rovibrational line ratios, H_2(2–1) S(1)/H_2(1–0) S(1) vs. H_2(1–0) S(2)/H_2(1–0) S(0). Ratios with H_2(2–1) S(1)/H_2(1–0) S(1) $\lesssim$0.2 indicate predominantly thermal excitation, while ratios $\gtrsim$0.5 are characteristic of nonthermal excitation dominated by UV fluorescence (H. Mouri 1994). The black points connected by dotted lines represent LTE predictions for temperatures between 1000 and 4000 K (R. A. Riffel 2021). The pink shaded region corresponds to AGN photoionization (O. L. Dors et al. 2012), the gray diamond symbols mark shock-excited regions (J. H. Kwan et al. 1977; M. D. Smith 1995), and the blue shaded region denotes thermal UV excitation (A. Sternberg & A. Dalgarno 1989). The brown star symbols indicate thermal X-ray excitation (B. T. Draine & D. T. Woods 1990). The solid black square with error bars represents the measured line ratios for NGC 4395.

$$L'_{\mathrm{CO}} = 3.25 \times 10^{7} \left(\frac{S_{\mathrm{CO}}\Delta v}{\mathrm{Jy\ km\ s^{-1}}}\right)\left(\frac{\nu_{\mathrm{obs}}}{\mathrm{GHz}}\right)^{-2} \times \left(\frac{D_L}{\mathrm{Mpc}}\right)^{2}(1+z)^{-3}. \quad (2)$$

Since the observed transition is CO(2–1), we convert this luminosity to its CO(1–0) equivalent using a line ratio of 1.66 as found by other Seyferts (A. Bewketu Belete et al. 2021). The resulting CO(1–0) luminosity is then multiplied by the standard CO-to-H_2 conversion factor of

$\alpha_{\rm CO} = (0.8 - 3.2)\, M_\odot\, ({\rm K\, km\, s^{-1}\, pc^2})^{-1}$ (A. Bewketu Belete et al. 2021), which strongly depends on the metallicity (D. Narayanan et al. 2012; F. Salvestrini et al. 2022), to obtain the total cold molecular gas mass. Following this method, we find that the total cold molecular gas has a mass of (0.95–3.2) × $10^6\, M_\odot$.

So, this warm/hot molecular gas mass (>500 K) to cold molecular gas mass (<100 K) is ratio 2.4–9.8) × 10^{-4}, but hot molecular (>1000 K), i.e., considering the hot and very hot component to cold molecular gas ratio (1.6–6.5) × 10^{-6}, which is in the range that found in other Seyferts (R. A. Riffel et al. 2020).

Then, we calculated the warm/hot molecular gas(>500 K) mass-to-ionized gas mass ratio, $M_{\rm H_2}/M_{\rm ion}$, and found that it is 0.7–0.9. This is consistent with values reported in the literature, for instance, in NGC 7319, M. Pereira-Santaella et al. (2022) observed a similar ratio, indicative of active feedback processes where the ionized phase can rival or exceed the warm/hot molecular mass content.

3.6. Excitation Mechanisms of the PAH and H_2 Features

We further investigated the excitation mechanism responsible for the detected PAH features to determine whether the observed emission is primarily associated with star formation or modified by AGN-related processes. From the measured PAH bands, we derive intensity ratios of $\rm PAH_{3.3}/PAH_{11.3} = 0.18 \pm 0.08$ and $\rm PAH_{6.2}/PAH_{11.3} = 0.97 \pm 0.07$. These relatively low ratios indicate a PAH population that is predominantly neutral and biased toward larger molecular sizes ($\gtrsim$200 carbon; D. Rigopoulou et al. 2024). Such conditions are consistent with the survival of robust, less-ionized grains in environments exposed to a hard radiation field, where small PAH molecules are preferentially destroyed or ionized.

The 7.7 and 12.7 μm features are typically associated with smaller and more ionized PAH molecules, and their absence indicates that the emission is dominated by large, neutral PAHs that can withstand the harsher AGN radiation field.

Recent spatially resolved JWST studies have reported similar behavior in several nearby active galaxies. The nuclear regions of Seyferts and LINERs often exhibit a suppression of the shorter-wavelength (ionized) PAH bands and an enhancement of the 11.3 μm feature, indicative of a higher neutral PAH fraction (e.g., K. M. Sandstrom et al. 2023; I. García-Bernete et al. 2024; D. Rigopoulou et al. 2024). Such trends are interpreted as the result of PAH processing by intense radiation fields or shocks, leading to the preferential survival of large neutral PAH molecules in the edges of the torus.

We investigated the excitation mechanism of the warm molecular gas through mid-infrared H_2-to-PAH diagnostics. The $\rm H_2\,S(3)\,(0–0)/PAH_{11.3}$ ratio was found to be −0.03 in logarithmic scale, placing the source firmly within the AGN-ionized regime. This suggests that the H_2 emission is primarily powered by shock excitation rather than UV heating from star-forming regions. Similar elevated H_2/PAH ratios have been reported in nearby radio-loud Seyferts such as 3C 293 and NGC 3884, where AGN jets and outflows interact strongly with the surrounding ISM (E. L. Lambrides et al. 2019; I. García-Bernete et al. 2024; D. E. Delaney et al. 2025; R. A. Riffel et al. 2025).

We further evaluated the [Fe II] 5.34 μm/$\rm PAH_{11.3}$ ratio, a well-known tracer of shocks in partially ionized gas. We obtained a value of −0.6 (log scale), which is comparable to those measured in the nuclei of 3C 293 and CGCG 012–070 (R. A. Riffel et al. 2025). Elevated [Fe II]/PAH ratios typically signal enhanced mechanical heating, where shocks release Fe from dust grains, leading to stronger [Fe II] emission relative to PAH features. Similar trends have been reported in various Seyfert and LINER galaxies (e.g., E. L. Lambrides et al. 2019), reinforcing the association between AGN-driven feedback and shock excitation of the ISM.

Taken together, the combination of low $\rm PAH_{6.2}/PAH_{11.3}$ and $\rm PAH_{3.3}/PAH_{11.3}$ ratios, the absence of the 7.7 and 12.7 μm features, and the elevated H_2/PAH and [Fe II]/PAH ratios point to a scenario where the PAH-emitting regions are dominated by shocks associated with AGN activity rather than photoionization from ongoing star formation. This interpretation is consistent with other jet–ISM interaction systems, where mechanical feedback from AGN outflows enhances molecular hydrogen emission while simultaneously suppressing or destroying the smallest PAH carriers. Such shock-dominated conditions illustrate the significant impact of AGN feedback on the excitation and chemical state of the circumnuclear ISM, even in systems with modest radiative luminosities.

4. Discussion

4.1. Multiphase Outflows

Our spectral decomposition analysis revealed that several fine-structure and molecular emission lines required more than a single-Gaussian component to achieve statistically robust fits. This additional broadened and velocity-shifted component is indicative of a kinematically distinct gas population consistent with outflowing material. The detection of these features across a broad range of ionization states and gas temperatures strongly supports the presence of multiphase outflows driven by AGN activity in NGC 4395, which is shown in Figure 6.

4.1.1. Ionized Gas Outflows

Clear signatures of outflows are observed across a broad range of ionized gas tracers in our data, spanning from low to high-IP species. The most prominent evidence for fast nuclear outflows comes from coronal lines such as [Fe VII], [Mg VIII], and [Si IX], which are formed in gas with IPs exceeding 100 eV. These lines display broad, asymmetric profiles and require the addition of secondary kinematic components with velocity shifts of several hundred km $\rm s^{-1}$ relative to systemic. Such features are characteristic of fast, highly ionized winds originating from the inner regions of the AGN, potentially close to the accretion disk or the base of the ionization cone (A. Rodríguez-Ardila et al. 2002; F. Müller-Sánchez et al. 2011; A. Rodríguez-Ardila et al. 2025).

In addition to the prominent high-ionization coronal lines, we identified broadened and blueshifted components in several low- to intermediate-ionization forbidden lines, including [Ar II] (IP ∼15.8 eV), [Ne II] (∼21.6 eV), and [Ca IV] (∼50.9 eV). These features point to the presence of ionized outflows that extend well beyond the innermost coronal region, impacting the NLR and potentially influencing the larger-scale ISM of the host galaxy.

The observed kinematic signatures in low-ionization lines are particularly noteworthy, as they offer a crucial window into

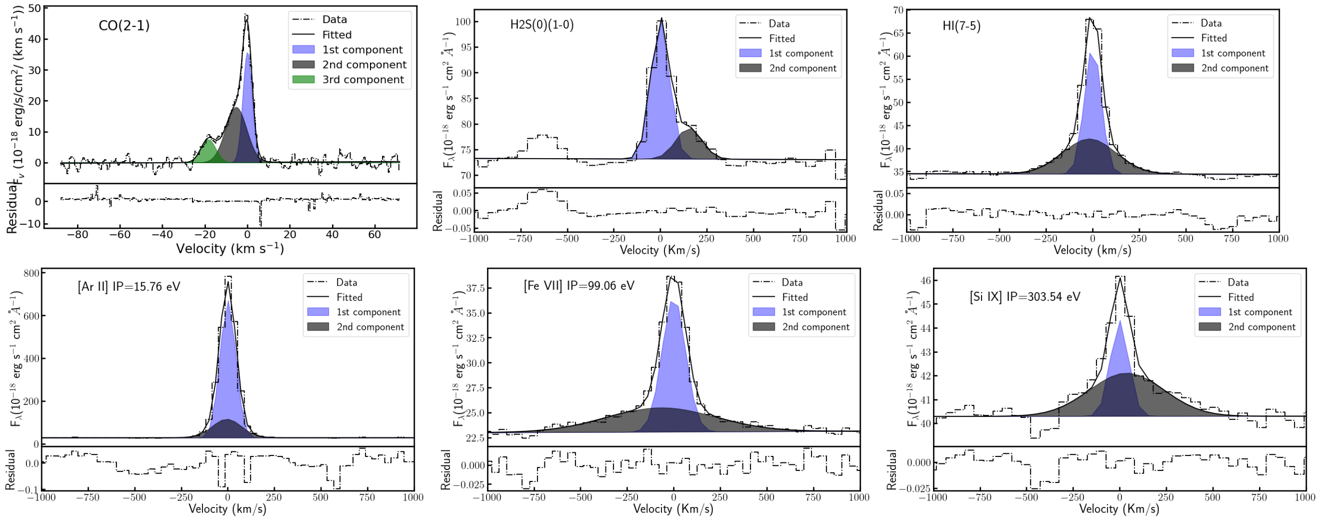

Figure 6. Visualization of outflows across multiple ionized gas phases: top panels show cold molecular gas (top left), hot molecular gas (top middle), and neutral HI gas (top right). The bottom panel illustrates ionized outflows traced by different elements spanning a range of ionization states, from low (left) to highly ionized gas (right). Corresponding spectral lines and IP are indicated in each panel.

the more extended and less extreme regions of the outflow. These lines are less affected by the extreme ionizing conditions near the nucleus, and their detection implies that the AGN-driven winds are capable of entraining and accelerating gas located farther from the central engine. Such findings are consistent with MIR IFU studies that demonstrate spatially resolved outflows extending over hundreds of parsecs to kiloparsec scales in nearby Seyferts and quasars (M. Pereira-Santaella et al. 2022; J. Álvarez-Márquez et al. 2023; L. Zhang et al. 2024).

Furthermore, we detected outflow components in [Fe II] lines, which are known to be enhanced in the presence of shocks due to their efficient excitation via collisional processes in partially ionized zones (E. Oliva et al. 2001; M. Mizumoto et al. 2024; T. Storchi-Bergmann et al. 2009). The presence of these features suggests a possible contribution from shock-induced ionization in addition to photoionization by the AGN, reinforcing a multiphase picture of AGN feedback that involves both radiative and mechanical drivers.

This diversity in ionization states and spatial extents implies a stratified, multiphase outflow structure, where the acceleration and ionization conditions vary with gas density, composition, and distance from the AGN. Gas with differing ionization states and densities responds variably to the AGN radiation field and mechanical forces (D. B. Fielding & G. L. Bryan 2022). Similar stratification has been reported in nearby Seyfert galaxies and luminous quasars (D. S. N. Rupke & S. Veilleux 2013; R. A. Riffel 2021; L. Armus et al. 2023; C. Marconcini et al. 2025), where compact, fast outflows in highly ionized lines coexist with more extended, slower flows traced by lower-ionization species. Our findings reinforce this scenario, showing that outflows traced by [Ne II], [Mg VII], [Si IX], and other MIR lines can effectively probe the kinematics of ionized gas phases otherwise inaccessible due to optical extinction.

To characterize the kinematics of the ionized outflowing gas, we computed the outflow velocity ($V_{\rm out}$) for each fine-structure line with outflows using the standard formalism: $V_{\rm out} = V_{\rm shift} + 2\sigma_{\rm out}$, where $V_{\rm shift}$ is the velocity offset between the broad (outflowing) and the narrow (systemic) components, and $\sigma_{\rm out}$ is the velocity dispersion of the broad component (corrected for instrumental effects). This definition accounts for both the bulk motion and the internal turbulent broadening of the outflow and is widely adopted in studies of AGN-driven winds (e.g., P. Nandi et al. 2025; E. Parlanti et al. 2025).

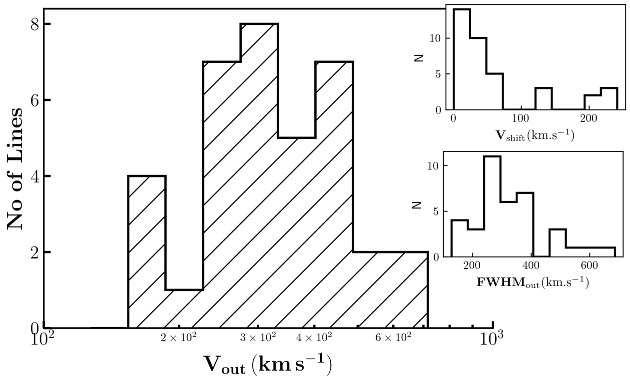

Figure 7. Distribution of the outflow velocity, $V_{\rm out}$ ($V_{\rm out} = V_{\rm shift} + 2\sigma_{\rm out}$), of ionized gas traced by fine-structure lines. The insets show the velocity shift ($V_{\rm shift}$) and the FWHM ($\text{FWHM}_{\rm out} = 2.355 \times \sigma_{\rm out}$) of the outflowing components.

The computed $V_{\rm out}$ range between 127 and 716 km s^{-1}, with a median value of 318 km s^{-1}. The distribution is illustrated in Figure 7. Notably, a subset of lines shows elevated outflow velocities ($V_{\rm out} > 400$ km s^{-1}), predominantly associated with shock-excited [Fe II] emission and high-ionization coronal lines such as [Fe VII], [Mg VII], and [Si IX]. These lines are expected to trace gas located closer to the active nucleus, where stronger radiation fields and mechanical feedback mechanisms, such as radiation pressure or jet-driven shocks, are capable of imparting higher momentum, resulting in faster outflowing material.

The observed velocities are consistent with typical values found in warm ionized outflows in nearby Seyfert galaxies (I. C. Freitas et al. 2018; D. Ruschel-Dutra et al. 2021; L. Gatto et al. 2024; P. Nandi et al. 2025), though they remain significantly below the velocities observed in UFOs detected in X-ray spectra, which can exceed 10,000 km s^{-1} (S. Laha et al. 2021). Together with the detection of lines spanning a wide range of IPs, this supports the presence of a stratified outflow structure, where different gas phases are accelerated to varying degrees depending on their density, ionization state, and distance from the central engine.

We estimated the mass of the ionized outflowing gas using the H I recombination lines and the formalism described in Section 3.4 (Equation 1), substituting the line luminosity with that of the broad outflowing H I component. The derived outflow masses are $M_{\rm out} = 503 \pm 35\,M_\odot$ and $370 \pm 82\,M_\odot$ from the Paα and Brγ lines, respectively. The corresponding mass outflow rates,[10] computed as $\dot{M}_{\rm out} = M_{\rm out}\,V_{\rm out}/R_{\rm out}$, are 0.03 $M_\odot$ $\rm yr^{-1}$ and 0.01 $M_\odot$ $\rm yr^{-1}$ for Paα and Brγ, respectively, adopting an outflow radius of $R_{\rm out} = 10.5$ pc (0.″5), which corresponds to the size of our spectral extraction aperture.

We further derived the ionized outflow mass using the high-ionization [Ne V] 14.32 μm line, adopting $n_e = 10^4$ $\rm cm^{-3}$ and $T_e = 1.5 \times 10^4$ K, and following Equation B5 of L. Zhang et al. (2024). In this calculation, we employed Paα instead of Pfα (used in L. Zhang et al. 2024), since Paα is the strongest H I transition in our line list. This yields $M_{\rm out} = 175 \pm 5\,M_\odot$.

Applying the same methodology as L. Zhang et al. (2024), and adopting identical assumptions,[11] We likewise estimated the outflowing mass traced by the high-ionization [Fe VII] 7.81 μm and [Mg VII] 3.03 μm lines, both of which show clear signatures of outflowing kinematics. Using the respective emissivities, we derived $M_{\rm out} = 112 \pm 40\,M_\odot$ from [Fe VII] and $M_{\rm out} = 178 \pm 21\,M_\odot$ from [Mg VII]. These values indicate that the total coronal-line outflowing mass lies in the range ∼110–180 $M_\odot$, with consistent estimates across all three high-ionization tracers. The corresponding mass outflow rate, $\dot{M}_{\rm out}$, is 0.002–0.006 $M_\odot$ $\rm yr^{-1}$.

The associated kinetic power of the outflow was calculated as

$$\dot{E}_{\rm out} = \frac{1}{2}\,\frac{M_{\rm out}}{R_{\rm out}}\,V_{\rm out}^3 \ {\rm erg\ s^{-1}}, \tag{3}$$

where we adopted $R_{\rm out} = 10.5$ pc (0.″5), corresponding to the size of our aperture. This gives $\dot{E}_{\rm out} = (2.71 \pm 0.19) \times 10^{39}$ erg s^{-1} for Paα and $(6.74 \pm 1.48) \times 10^{38}$ erg s^{-1} for Brγ.

Similarly, we derived $\dot{E}_{\rm out} = (6.38 \pm 1.38) \times 10^{36}$ erg s^{-1} from [Ne V], $(1.90 \pm 0.78) \times 10^{38}$ erg s^{-1} from [Fe VII], and $(2.41 \pm 0.38) \times 10^{38}$ erg s^{-1} from [Mg VII]. The outflow energetics inferred from [Fe VII] and [Mg VII] are over an order of magnitude higher than those derived from [Ne V], yet about an order of magnitude lower than those from the low-ionization H I lines. This suggests that [Fe VII], which traces a more powerful outflow, likely originates closer to the central engine than [Ne V], as it is associated with denser gas (see Section 3.3). In contrast, the lower-ionization outflows, characterized by lower densities, likely arise farther from the nucleus where the gas interacts more strongly with the surrounding ISM.

In all cases, the kinetic power of the outflow remains several orders of magnitude below the AGN bolometric luminosity, $(1.95\text{–}4.97) \times 10^{41}$ erg s^{-1}, and also lower than the estimated jet power, $(1.3 \pm 0.3) \times 10^{40}$ erg s^{-1} (P. Nandi et al. 2023b). The corresponding kinetic coupling efficiencies, defined as $\dot{E}_{\rm out}/L_{\rm bol}$, range between 0.4%–1.4% for the low-ionization H I lines and 0.003%–0.12% for the coronal-line outflows, assuming the lower limit of $L_{\rm bol} = 1.95 \times 10^{41}$ erg s^{-1}.

These efficiencies are consistent with the theoretical threshold for H I outflows but fall well below the ∼1% level expected for the coronal-line outflows to drive significant AGN feedback capable of regulating star formation (C. M. Harrison et al. 2018). This suggests that the low-ionization outflows can more effectively influence the surrounding ISM of the host galaxy than the coronal-line outflows.

4.1.2. Outflows in Molecular Gas

Beyond the ionized gas phases, we also found evidence of outflows in the warm and hot molecular gas components. A prominent example is the H_2(1–0) S(0) rovibrational line at 2.2245 μm, which exhibits a secondary broadened kinematic component with a velocity shift of ∼154 km s^{-1} relative to the narrow component and a FWHM of 163 km s^{-1}. This line is known to trace hot ($T \sim$ a few 1000 K) molecular gas, typically excited by shocks or intense radiation fields in AGN environments (e.g., M. J. Hill & N. L. Zakamska 2014; A. J. Richings & C.-A. Faucher-Giguère 2018). The detection of this broadened component supports the presence of AGN-driven molecular outflows in the nuclear region of the galaxy.

In addition to this rovibrational line, signatures of molecular outflows were also found in several pure rotational H_2 transitions observed in the mid-infrared. For warm molecular gas, we detected outflow components in the H_2 S(2), S(3), S(4), and S(5) (0–0) lines. These exhibit low velocity offsets (<10 km s^{-1}) but are broadened, with FWHM values of 121, 146, 111, and 106 km s^{-1}, respectively. Furthermore, we identified an outflow component in the H_2(0–0) S(8) line at 5.0353 μm, which shows a velocity shift of ∼10 km s^{-1} and a broader profile with FWHM ∼180 km s^{-1}, indicative of a hotter molecular gas phase. These findings are consistent with previous observations of warm molecular outflows in AGN (e.g., F. M. Maccagni et al. 2016; M. Pereira-Santaella et al. 2022; J. H. Costa-Souza et al. 2024; R. A. Riffel et al. 2025), reinforcing the multiphase nature of AGN feedback and its influence on the host galaxy's molecular ISM.

We detected outflows in several H_2 transitions, including the pure rotational S(2)–S(5) (0–0) lines and the rovibrational H_2(1–0) S(0) line at 2.22 μm, but not in the stronger H_2(1–0) S(1) line at 2.12 μm. This differential detection reflected their distinct excitation conditions (upper level excitation energy for H_2(1–0) S(0) is 6471 K and H_2(1–0) S(1) is 6956 K (I. Dabrowski 1984)). The H_2(1–0) S(1) line is often associated with warm molecular gas that can be excited by UV fluorescence, shocks, or X-ray heating (J. H. Black & E. F. van Dishoeck 1987; P. R. Maloney et al. 1996). However, for this source, the measured rovibrational line ratios (see lower panel of Figure 5) place the emission firmly in the *thermal excitation region* of the diagnostic diagram of H. Mouri (1994), rather than in the nonthermal UV-fluorescent regime. This indicates that the dominant excitation mechanism is thermal, collisional heating, most plausibly driven by shocks associated with the outflow interacting with the surrounding ISM, rather than radiative UV pumping.

---

[10] These are lower limits, as we considered the outflow radius as 0.″5, which is mostly an upper limit.

[11] The emissivities of the relevant transitions vary by less than 1% across densities of 10^3–10^4 $\rm cm^{-3}$. These emissivities were obtained from the CHIANTI database: https://www.chiantidatabase.org/chianti_chiantipy.html.

We estimated the warm/hot molecular outflow mass by computing the fraction of outflowing flux (f) relative to the total flux of the rovibrational H_2 (1–0) S(0) line, obtaining $f = 0.24$. This yields an outflowing molecular mass of $f \times M\text{mol} = 223\, M_\odot$. Using the outflow velocity derived from the H_2(1–0) S(0) outflow component (223 km s^{-1}), we infer a mass outflow rate of 0.005 $M_\odot$, yr^{-1}. The corresponding kinetic power, $\dot{E}_{\rm out}$, is 1.07×10^{38} erg, s^{-1}, consistent with the value obtained from the coronal-line outflow.

In addition to the ionized, hot, and warm molecular phases, signatures of outflows are also evident in the cold molecular gas component, as traced by the CO(2–1) rotational transition at 1.3 mm observed with ALMA. The CO(2–1) line profile reveals a complex kinematic structure composed of three distinct components: a narrow, systemic component, and two broader components blueshifted with respect to the systemic velocity, indicative of cold molecular outflows as shown in the upper left panel of Figure 6.

The total integrated flux of the CO(2–1) line is measured to be 4.84×10^{-16} erg s^{-1} cm^{-2}. The line profile reveals a narrow systemic component with a flux of 1.95×10^{-16} erg s^{-1} cm^{-2} and a FWHM of 5.1 km s^{-1}, consistent with dynamically cold, gravitationally bound gas. In addition, two outflowing components are detected, with fluxes of 2.23×10^{-16} and 0.65×10^{-16} erg s^{-1} cm^{-2}, blueshifted by 5.3 km s^{-1} and 18.4 km s^{-1} relative to the systemic component, and FWHMs of 11.71 km s^{-1} and 8.2 km s^{-1}, respectively. The detection of multiple velocity components in the CO(2–1) line suggests a stratified or multiphase outflow structure, potentially tracing distinct spatial zones or evolutionary stages of gas entrainment and acceleration. Similar structured outflows in the cold molecular phase have been observed in other AGN-hosting systems (e.g., A. Fluetsch et al. 2019; B. Dall'Agnol de Oliveira et al. 2023), underscoring the impact of AGN-driven winds on even the densest and coldest regions of the ISM.

These relatively narrow line widths suggest that the cold molecular gas traced by CO(2–1) is less turbulent than the warm or hot molecular components. The kinematics of this cold gas differ substantially from those of the warm/hot molecular outflow traced by the H_2 lines. Moreover, the cold CO-emitting gas is displaced by ~20 pc from the nucleus, in a direction perpendicular to the AGN jet toward the north direction (P. Nandi et al. 2023b), whereas the warm and hot molecular gas is concentrated in the central region coincident with the jet. This spatial and kinematic decoupling implies that the warm/hot molecular component may not share the same origin as the cold molecular gas.

Using the CO(2–1) line and Equation 2, together with the prescriptions outlined in the previous section, we estimated the mass of the outflowing cold molecular gas from the velocity-integrated fluxes of the two outflow components. The total cold molecular outflow mass is $(0.57–2.27) \times 10^6\, M_\odot$, with the first component contributing $(0.44–1.76) \times 10^6\, M_\odot$ and the higher-velocity component contributing $(0.13–0.51) \times 10^6\, M_\odot$. The corresponding mass outflow rates are $(0.31–1.25)\, M_\odot\, \text{yr}^{-1}$ for the first component and $(0.15–0.61)\, M_\odot\, \text{yr}^{-1}$ for the second. These values are significantly higher than the outflow rates derived for the warm/hot molecular and ionized gas phases. The associated kinetic powers are $(2.08–8.33) \times 10^{37}$ erg s^{-1} and $(2.85–11.4) \times 10^{37}$ erg s^{-1} for the first and second components, respectively.

By comparing the outflow signatures across different gas phases and their velocity shifts relative to the narrow disk component, the overall pattern reveals a stratified, multiphase outflow shaped by phase-dependent obscuration. Most fine-structure ionized lines, along with the intermediate-ionization coronal lines [Fe VII] and [Si VII], exhibit blueshifted components, consistent with emission from an unobscured near-side outflow. In contrast, the very high-ionization coronal line [Si IX] and the H_2 molecular lines are redshifted, implying that their near-side emission is attenuated by nuclear dust or the inner torus, leaving the receding component dominant. Such ionization-dependent velocity behavior indicates that different species originate at different radii and encounter varying levels of extinction, consistent with a biconical outflow geometry—already spatially resolved for the [O III] outflow using HST by P. Nandi et al. (2023b). Similar stratified and obscured biconical structures have been reported in other AGN (e.g., D. M. Crenshaw et al. 2009; F. Müller-Sánchez et al. 2011; T. C. Fischer et al. 2013), supporting a scenario in which the observed kinematics of each gas phase depend on both its location within the outflow and the line-of-sight extinction.

4.2. IP Dependence of Outflow Properties

To probe the physical and ionization structure of the ionized outflows, we explored the relationship between the kinematic properties of the emitting gas and the IP of the corresponding ionic species. The IP serves as a proxy for the ionization state and can reveal the stratification in both energy and spatial origin within the outflowing medium (e.g., A. Rodríguez-Ardila et al. 2002; C. Cicone et al. 2014).

We initially examined the relationship between the outflow velocity and the IP of each emission line. No statistically significant correlation was found (Pearson correlation coefficient $r = 0.20$, $p = 0.34$), suggesting that the kinematics of the outflowing gas are largely independent of the ionization state of the emitting species. Notably, the [Fe,II] lines (IP ~7.9 eV) display systematically higher $V_{\rm out}$. When these [Fe,II] lines are excluded, a positive correlation emerges ($r = 0.47$, $p = 0.031$; which is shown in the upper panel of Figure 8), in agreement with previous studies (A. Rodríguez-Ardila et al. 2002; H. Inami et al. 2013). This behavior indicates that [Fe,II], which is strongly enhanced in shocked regions, deviates from the general IP–$V_{\rm out}$ trend and likely traces a distinct shock-driven kinematic component of the outflow (e.g., E. Oliva et al. 2001; A. Rodríguez-Ardila et al. 2004).

In the lower panel of Figure 8, we present the ratio of outflow flux to total line flux ($F_{\rm out}/F_{\rm total}$) as a function of the IP. This ratio shows a statistically significant positive trend (Pearson correlation coefficient $r = 0.49$, $p = 0.01$) similar to the finding of L. Armus et al. (2023) for NGC 7469, suggesting that lines from more highly ionized species tend to exhibit a stronger outflow component. This trend is becoming more prominent after excluding [Fe II] lines with a Pearson correlation coefficient $r = 0.69$, $p = 0.0006$. This trend supports the presence of an ionization stratification in which higher-ionization gas is more effectively coupled to outflowing motions, possibly originating from regions closer to the active nucleus where radiation pressure or mechanical feedback is stronger (C. M. Harrison et al. 2018; M. Pereira-Santaella et al. 2022; M. A. Fonseca-Faria et al. 2023). This excess in $V_{\rm out}$ and $F_{\rm out}/F_{\rm total}$ suggests a distinct

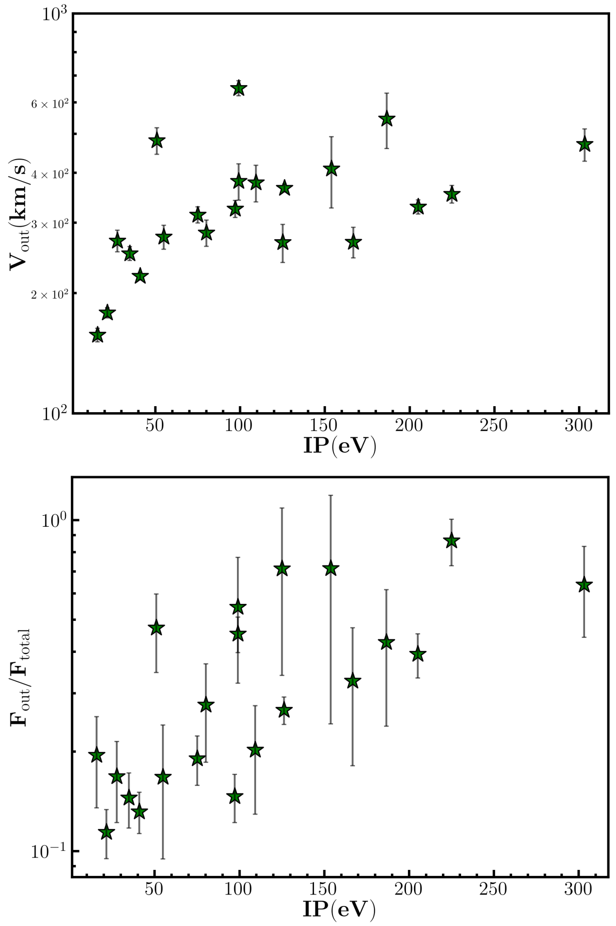

Figure 8. Variation in outflow velocity ionized gas (top), outflow flux to total flux ratio (lower; excluding [Fe II] lines) with IP.

excitation mechanism for [Fe II], likely dominated by shocks rather than photoionization, consistent with previous studies highlighting the shock sensitivity of [Fe II] emission in AGN environments (e.g., M. Contini & S. M. Viegas 1991; B.-C. Koo et al. 2016; M. Mizumoto et al. 2024).

We also attempted to assess how the outflow kinetic power might scale with IP. Although a complete calculation of the kinetic power requires knowledge of the n_e and T_e of each ion, parameters that vary significantly with the ionization state and are not uniformly constrained for all species, an approximate indicator can be derived from $KP_{\rm out} \propto L_{\rm out} V_{\rm out}^3$. We therefore computed this proxy for each line and examined its dependence on IP. As shown in Figure 9, the resulting trend suggests a weak negative correlation (Pearson $r = -0.260$, $p = 0.24$), with hints of decreasing $KP_{\rm out}$ at higher IP. This may reflect either a reduced mass-loading factor in more ionized gas.

Overall, these results point to a stratified, multiphase outflow where the coupling of AGN-driven forces is more effective in highly ionized gas, while the kinetic power may be distributed across different ionization zones with varying efficiency.

The collective detection of outflows in ionized, hot molecular, warm molecular, and cold molecular gas provides compelling evidence for a multiphase outflow in NGC 4395. These components span a wide range of temperatures (from $\sim 10^2$ to 10^6 K) and ionization states, underscoring the diverse impact of AGN-driven winds on the surrounding ISM. The velocity structure and line profile asymmetries vary significantly between gas phases, reflecting differences in acceleration mechanisms, gas densities, and spatial origin. These observations demonstrate that even a low-luminosity AGN in a dwarf galaxy can drive complex, multiphase outflows, contributing to the regulation of gas dynamics and potentially influencing future star formation in the host.

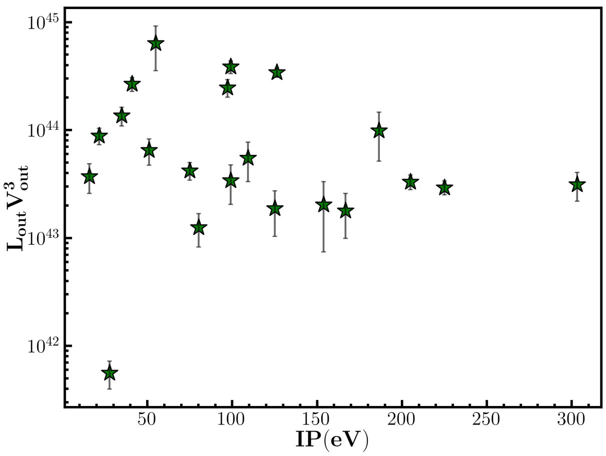

Figure 9. Variation in $L_{\rm out} V_{\rm out}^3$ with IP. $L_{\rm out} V_{\rm out}^3$ is in the unit of erg s^{-1} (km s^{-1})^3.

5. Summary and Conclusions

In this work, we present a comprehensive multiwavelength analysis of the nearby dwarf Seyfert galaxy NGC 4395, hosting an IMBH, based on spatially resolved spectroscopy from JWST/NIRSpec and MIRI, ALMA, and Gemini/GMOS. Our key findings are summarized as follows:

1. We detected 134 emission lines, including H I recombination lines (Paschen, Brackett, Pfund, and Humphreys series), He I and He II lines, fine-structure lines from both low- and high-ionization species (e.g., [Fe II], [Ne V], [Si IX], [Mg VIII]) with IP ranges from 7.6 to 300 eV, and pure rotational and rovibrational H_2 lines. We also detected a few distinct continuum features of PAH, 3.3 μm, 6.2 μm, 11.3 μm, and a PAH plateau in the 15–20 μm region.
2. Using a suite of diagnostics from [Fe II], [Fe VII], and [Ne V], we found a clear stratification in electron density (n_e) and temperature (T_e), with higher values associated with Fe lines.
3. We found that molecular H_2 gas consists of three phases of gas. The warm phase of $T \approx 580$ K, the hot phase of $T \approx 1480$ K, and the very hot gas phase of $T \approx 2900$ K.
4. The PAH emission is dominated by large, neutral molecules, as indicated by the low PAH3.3/PAH11.3 and PAH6.2/PAH11.3 ratios and the absence of the 7.7 and 12.7 μm bands. This pattern reflects strong AGN processing, where small PAHs are destroyed, and only the more resilient neutral PAHs survive.
5. From hydrogen recombination lines, we estimated an ionized gas mass of $M_{\rm ion} \approx 1200\ M_\odot$, under Case B conditions, and molecular hydrogen mass (936 $M_\odot$).
6. Multiphase outflows are detected across different ionized species through fine-structure lines, H I, and molecular gas through H_2 lines.

7. Outflow signatures appear in 36 fine-structure lines, multiple H_2 transitions, and the CO(2–1) line. Ionized outflows traced by both low-ionization ([Fe II], [Ar II]) and high-ionization coronal lines ([Mg VIII], [Si IX]) exhibit stratified kinematics. Outflow velocities span 127–716 km s^{-1}, with higher velocities generally observed in high-ionization or shock-sensitive lines such as [Fe II], [Mg VIII], and [Si IX].
8. Cold molecular outflows are identified through kinematic decomposition of ALMA CO(2–1) emission, revealing distinct blueshifted components with lower velocity dispersions than the warm/hot molecular gas or ionized phase, but carrying a substantial gas mass component.
9. The ionized outflow masses estimated from the H I lines are in 370–500) $M_\odot$, whereas for high-ionization tracers, we derived significantly lower outflow masses: 110–180 $M_\odot$.
10. The outflow rate for cold molecular gas is 0.15–1.25 $M_\odot$ yr^{-1}, which is much higher than warm/hot molecular outflow (lower limit; 0.005 $M_\odot$ yr^{-1}) or ionized outflows (lower limit; 0.002–0.006 $M_\odot$ yr^{-1} for coronal outflows and 0.01–0.03 $M_\odot$ yr^{-1} for H I outflows).
11. The kinetic coupling efficiencies for ionized outflows range from 0.4%–1.4% for the low-ionization H I lines outflows and 0.003%–0.12% for the coronal-line outflows, well below the ∼1% threshold generally considered necessary for AGN feedback to strongly suppress star formation in the host galaxy.
12. We found a positive correlation between both the fraction of flux in the outflowing component and outflow velocity with the IP of the emission lines, supporting the scenario of radially stratified AGN-driven feedback, where higher-ionization gas closer to the nucleus is more efficiently accelerated. Notably, [Fe II] lines deviate from this trend, likely reflecting their dominant excitation by shocks rather than photoionization, consistent with their known sensitivity to shock-heated gas.

These results collectively demonstrate that even low-luminosity AGN hosted in dwarf galaxies can drive complex, multiphase outflows and exert significant influence on their local ISM. Our findings underscore the importance of high-resolution infrared and millimeter interferometry in disentangling the structure and impact of AGN feedback in low-mass galaxies.

Acknowledgments

We thank the anonymous reviewer for the encouraging and constructive comments, which helped to improve our manuscript. This work is based [in part] on observations made with the NASA/ESA/CSA James Webb Space Telescope. The data were obtained from the Mikulski Archive for Space Telescopes at the Space Telescope Science Institute, which is operated by the Association of Universities for Research in Astronomy, Inc., under NASA contract NAS 5-03127 for JWST. These observations are associated with program ID 2016. This work is partly based on observations obtained at the Gemini Observatory, which is operated by the Association of Universities for Research in Astronomy, Inc., under a cooperative agreement with the NSF on behalf of the Gemini partnership: the National Science Foundation (United States), the Science and Technology Facilities Council (United Kingdom), the National Research Council (Canada), CONICYT (Chile), the Australian Research Council (Australia), Ministério da Ciência e Tecnologia (Brazil) and southeast CYT (Argentina). This paper makes use of the following ALMA data: ADS/JAO.ALMA#2017.1.00572.S. ALMA is a partnership of ESO (representing its member states), NSF (USA) and NINS (Japan), together with NRC (Canada), MOST and ASIAA (Taiwan), and KASI (Republic of Korea), in cooperation with the Republic of Chile. The Joint ALMA Observatory is operated by ESO, AUI/NRAO, and NAOJ. This work has made use of the NASA Astrophysics Data System (ADS)[12] and the NASA/IPAC extragalactic database (NED).[13] PN would like to thank the COSPAR Capacity Building Programme for the support toward visiting CAB to start and complete a major part of this work. RAR acknowledges the support from Conselho Nacional de Desenvolvimento Científico e Tecnológico (CNPq; Proj. 303450/2022-3, 403398/2023-1, & 441722/2023-7) and Coordenação de Aperfeiçoamento de Pessoal de Nível Superior (CAPES; Proj. 88887.894973/2023-00). MPS acknowledges support under grants RYC2021-033094-I, CNS2023-145506, and PID2023-146667NB-I00 funded by MCIN/AEI/10.13039/501100011033 and the European Union NextGenerationEU/PRTR. J.A.-M. acknowledges support by grants PIB2021-127718NB-100 & PID2024-158856NA-I00 from the Spanish Ministry of Science and Innovation/State Agency of Research MCIN/AEI/10.13039/501100011033 and by "ERDF A way of making Europe."

Author Contributions

The first author conducted the data reduction and analysis and led the writing of the manuscript. The coauthors contributed to the interpretation of the results and provided detailed, constructive feedback that shaped the manuscript into its current form.

Facilities: JWST (NIRSpec and MIRI), ALMA, Gemini: Gillett (GMOS).

Software: Numpy (C. R. Harris et al. 2020), Astropy (Astropy Collaboration et al. 2022, 2013, 2018), Scipy (P. Virtanen et al. 2020), Matplotlib (J. D. Hunter 2007), PyNeb (V. Luridiana et al. 2015), PDR M. W. Pound & M. G. Wolfire (2023, 2008); M. J. Kaufman et al. (2006); M. W. Pound & M. G. Wolfire (2011) .

Appendix A
Instrumental Resolution

The instrumental resolutions of NIRSpec and MIRI are compared with the measured line widths, shown as labeled data points in the figure A1. In the left panel, the dotted curve represents our measurements, while the solid curves correspond to previously reported MIRI spectral resolutions from I. Argyriou et al. (2023), K. M. Pontoppidan et al. (2024), and A. Banzatti et al. (2025). In the right panel, we compare the resolving power derived from our observed NIRSpec lines (shown as dotted data points) with the expected instrumental resolution indicated by the blue and red curves, along with their shaded regions, which represent the 30% uncertainty reported on the JWST-NIRSpec documentation page.[14]

---

[12] https://ui.adsabs.harvard.edu/

[13] https://ned.ipac.caltech.edu

[14] https://jwst-docs.stsci.edu/jwst-near-infrared-spectrograph/nirspec-instrumentation/nirspec-dispersers-and-filters#gsc.tab=0

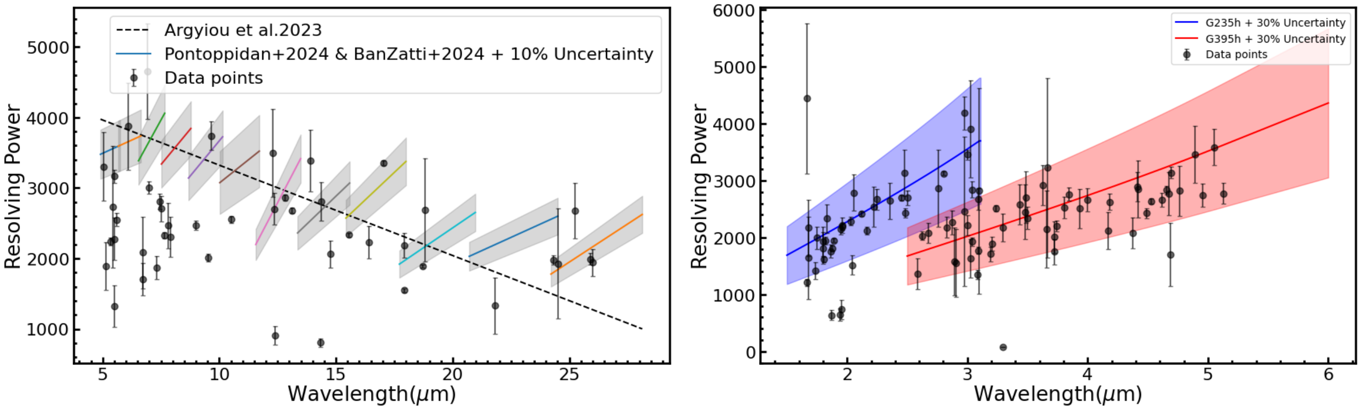

Figure A1. Variation in spectral resolving power with wavelength in MIRI (left panel) and NIRSpec (right panel).

Appendix B
Diagnosis for Electron Density and Temperature

Here in Figure B1 and B2, we examine a range of emission-line diagnostics to evaluate their reliability as tracers of n_e and T_e, identifying which indicators provide robust constraints and which are less effective under the physical conditions probed in this study.

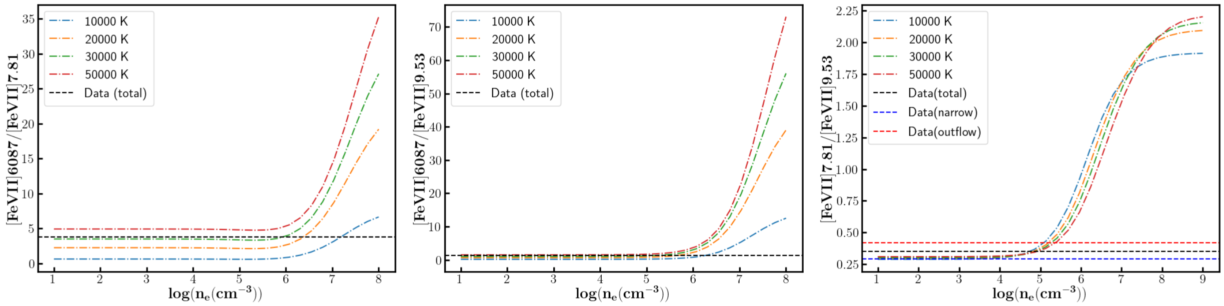

Figure B1. Variation in different line ratios with density for different particular temperatures, which represent different curves in each plot, and are denoted by individual legends in each plot. The horizontal line in each plot represents the observed line ratio.

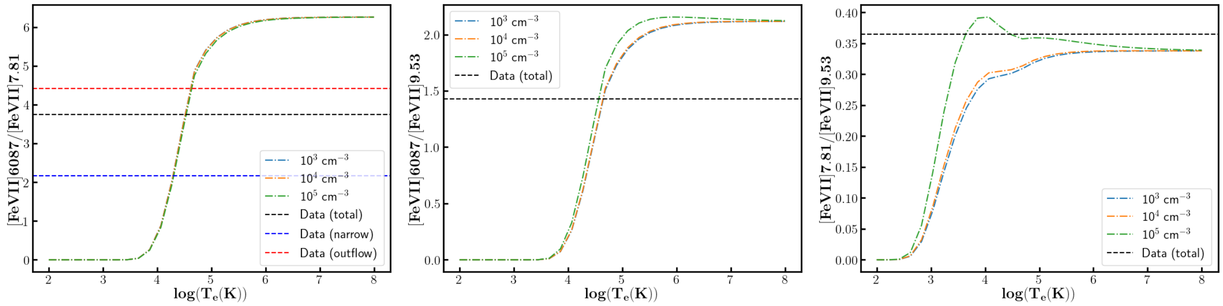

Figure B2. Variation in different line ratios with electron temperature for different particular electron densities, which represent different curves in each plot, and are denoted by individual legends in each plot. The horizontal line in each plot represents the observed line ratio.

Appendix C
Identified Lines

Here in Table C1, we list all the identified emission lines together with their IPs, wavelengths, and flux in the nuclear spectra.

Table C1
Emission-line Measurements Identified in the Nuclear Spectra

Line	IP (eV)	λ_{vac} (μm)	Flux $_{\mathrm{total}}$	Flux $^{err}_{\mathrm{total}}$
H I lines				
H I (11–4)	—	1.6811	4.2	1.6
H I (10–4)	—	1.7367	6.7	1.3
H I (9–4)	—	1.8179	7.9	0.5
H I (4–3)	—	1.8756	213.2	8.0
H I (8–4)	—	1.9451	11.4	0.9
H I (7–4)	—	2.1661	17.6	0.9
H I (6–4)	—	2.6259	28.1	1.8
H I (13–5)	—	2.6744	1.0	0.1
H I (12–5)	—	2.7583	2.1	0.7
H I (11–5)	—	2.8730	2.9	0.5
H I (10–5)	—	3.0392	3.7	0.4
H I (9–5)	—	3.2970	4.3	1.0
H I (8–5)	—	3.7406	6.6	0.6
H I (13–6)	—	4.1708	0.7	0.1
H I (12–6)	—	4.3765	1.2	0.3
H I (7–5)	—	4.6538	9.1	0.4
H I (11–6)	—	4.6725	2.0	0.4
H I (10–6)	—	5.1287	1.9	0.5
H I (9–6)	—	5.9082	3.2	0.9
H I (6–5)	—	7.4599	15.2	1.2
H I (8–6)	—	7.5025	4.5	0.6
H I (11–7)	—	5.5081	1.1	0.3
H I (7–6)	—	12.372	6.7	1.0
H I (11–8)	—	12.387	2.4	0.4
He lines				
He II	—	1.8642	8.9	0.8
He I	—	1.8690	12.0	2.2
He I	—	2.0587	2.5	0.4
He II	—	2.8260	1.2	0.9
He II	—	3.0908	4.3	0.5
He II	—	3.0917	3.9	0.2
He II	—	3.0955	0.2	0.1
He II	—	4.7635	1.8	0.8
H_2 lines				
H_2(1–0) S(7)	—	1.7481	2.3	0.1
H_2(1–0) S(6)	—	1.7880	1.6	0.1
H_2(1–0) S(5)	—	1.8358	4.3	1.1
H_2(1–0) S(4)	—	1.8920	1.79	0.04
H_2(1–0) S(3)	—	1.9576	7.4	0.3
H_2(1–0) S(2)	—	2.0338	3.0	0.1
H_2(1–0) S(1)	—	2.1218	8.8	0.2
H_2(1–0) S(0)	—	2.2235	3.3	0.7
H_2(2–1) S(1)	—	2.2477	1.2	0.1
H_2(2–1) S(0)	—	2.3556	0.6	0.1
H_2(1–0) Q(5)	—	2.4549	4.0	0.1
H_2(1–0) Q(6)	—	2.4756	1.1	0.2
H_2(1–0) Q(7)	—	2.5001	1.6	0.1
H_2(1–0) O(3)	—	2.8025	7.8	0.2
H_2(2–1) O(3)	—	2.9741	1.0	0.3
H_2(1–0) O(4)	—	3.0038	2.3	0.8
H_2(3–2) O(3)	—	3.1637	0.5	0.1
H_2(2–1) O(4)	—	3.1899	0.7	0.1
H_2(1–0) O(5)	—	3.2349	3.7	0.1
H_2(2–1) O(5)	—	3.4379	0.7	0.2
H_2(1–0) O(6)	—	3.5007	1.0	0.1
H_2(0–0) S(15)	—	3.6264	0.7	0.2
H_2(3–2) O(5)	—	3.6632	0.16	0.03
H_2(2–1) O(6)	—	3.7237	0.6	0.1
H_2(0–0) S(14)	—	3.7256	0.5	0.1
H_2(0–0) S(13)	—	3.8472	1.1	0.1
H_2(0–0) S(12)	—	3.9969	0.4	0.03
H_2(1–0) O(7)	—	3.8074	1.2	0.1
H_2(0–0) S(11)	—	4.1815	1.9	0.1
H_2(0–0) S(10)	—	4.4099	1.0	0.2
H_2(1–1) S(11)	—	4.4167	0.4	0.1
H_2(0–0) S(9)	—	4.6947	4.1	0.3
H_2(1–1) S(9)	—	4.9542	0.5	0.1
H_2(0–0) S(8)	—	5.0531	2.2	0.6
H_2(0–0) S(7)	—	5.5118	11.3	0.5
H_2(0–0) S(6)	—	6.1086	7.4	0.4
H_2(0–0) S(5)	—	6.9095	42.8	9.7
H_2(0–0) S(4)	—	8.0251	25.7	9.3
H_2(0–0) S(3)	—	9.6649	110.2	9.1
H_2(0–0) S(2)	—	12.279	59.6	5.3
H_2(0–0) S(1)	—	17.035	100.9	2.3
Fine-structure lines				
[Fe II]	7.9	1.6642	1.8	0.1
Fe I]	—	1.6684	2.2	0.7
[Fe II]	7.9	1.6773	3.9	0.6
[Fe II]	7.9	1.7976	1.3	0.3
[Fe II]	7.9	1.8005	2.1	0.7
[Fe II]	7.9	1.8094	7.3	0.5
[Ni II]	7.64	1.9393	2.4	0.5
[Fe II]	7.9	1.9541	1.2	0.4
[Si VI]	166.7	1.9634	11.5	1.8
[Fe II]	7.9	2.0465	1.0	0.2
[Si VII]	205.05	2.4833	9.6	0.6
[Si IX]	303.17	2.5842	1.7	0.2
[Mg VIII]	224.95	3.0279	3.1	0.3
[Fe V]	54.8	2.8934	0.8	0.3
[Fe III]	16.18	2.9049	0.7	0.3
[Mg VIII]	224.95	3.0279	2.2	0.8
[Fe II]	7.9	3.0816	1.9	0.1
[Ca IV]	50.91	3.2067	5.0	0.6
Fe I]	—	3.4831	0.27	0.07
Mg I]	—	3.4856	0.33	0.07
[Al VI]	153.83	3.6597	1.7	0.7
[Si IX]	303.17	3.9357	1.9	0.3
[Mg IV]	80.14	4.4867	8.1	0.7
[Ar VI]	75.02	4.5295	28.9	1.1
[K III]	31.63	4.6180	1.5	0.1
[Na VII]	172.15	4.6847	0.23	0.1
[Fe II]	7.9	4.8891	0.70	0.2
[Fe II]	7.9	5.3402	28.6	1.7
[Fe VIII]	125.1	5.4466	5.6	1.8
[Mg VII]	186.51	5.5032	5.8	1.2
[Mg V]	109.24	5.6098	20.5	1.7
[Ni II]	7.64	6.636	3.8	0.2
[Cl V]	53.46	6.7067	0.8	0.3
[Fe II]	7.9	6.7213	1.6	0.3
[Ar II]	15.76	6.9853	198.9	14.3
[Na III]	47.29	7.3177	1.6	0.2
[Ne VI]	126.21	7.6524	105.3	3.4
[Fe VII]	99.1	7.8145	4.6	0.3
[Ar V]	59.81	7.9016	11.7	1.5
[Ar III]	27.63	8.9914	0.68	0.04
[Fe VII]	99.1	9.5267	12.5	0.4
[S IV]	34.79	10.511	239.5	9.1
[Ne II]	21.56	12.814	550.3	16.8

Table C1
(Continued)

Line	IP (eV)	$\lambda_{\rm vac}$ (μm)	Flux $_{\rm total}$	Flux $^{err}_{\rm total}$
[Ar V]	59.81	13.102	16.8	2.7
[Mg V]	109.24	13.521	1.6	0.6
[Ne V]	97.12	14.322	199.7	6.7
[Fe VI]	75.0	13.906	0.58	0.15
[Cl II]	12.97	14.368	4.9	0.6
[Fe VI]	75.0	14.771	2.2	0.3
[Ne III]	40.96	15.555	764.2	19.3
[Co III]	17.08	16.407	0.94	0.28
[Fe II]	7.9	17.936	22.9	0.6
[S III]	23.34	18.713	308.5	8.5
[Co II]	17.08	18.804	0.97	0.33
[Ar III]	27.63	21.830	4.5	0.8
[Fe III]	16.19	22.925	4.7	0.7
[Ne V]	97.12	24.318	156.0	9.8
[Fe II]	7.9	24.519	7.7	0.9
[S I]	—	25.249	5.9	1.2
[O IV]	54.93	25.890	728.9	65.7
[Fe II]	7.9	25.988	31.0	4.3

Note. IP = Ionization potential of the corresponding ion; $\lambda_{\rm vac}$ = vacuum wavelength of the transition. The flux and flux error are in units of 10^{-16} erg s^{-1} cm^{-2}.

ORCID iDs

Payel Nandi https://orcid.org/0009-0003-9765-3517
Luis Colina https://orcid.org/0000-0002-9090-4227
Rogemar A. Riffel https://orcid.org/0000-0003-0483-3723
Miguel Pereira Santaella https://orcid.org/0000-0002-4005-9619
C. S. Stalin https://orcid.org/0000-0002-4998-1861
D.J. Saikia https://orcid.org/0000-0002-4464-8023
Javier Álvarez-Márquez https://orcid.org/0000-0002-7093-1877
Markus Kissler-Patig https://orcid.org/0000-0002-5908-1488

References

Allen, M. G., Groves, B. A., Dopita, M. A., Sutherland, R. S., & Kewley, L. J. 2008, ApJS, 178, 20
Álvarez-Márquez, J., Labiano, A., Guillard, P., et al. 2023, A&A, 672, A108
Arav, N., Chamberlain, C., Kriss, G. A., et al. 2015, A&A, 577, A37
Argyriou, I., Glasse, A., Law, D. R., et al. 2023, A&A, 675, A111
Armus, L., Lai, T., U, V., et al. 2023, ApJL, 942, L37
Astropy Collaboration, Price-Whelan, A. M., Lim, P. L., et al. 2022, ApJ, 935, 167
Astropy Collaboration, Price-Whelan, A. M., Sipőcz, B. M., et al. 2018, AJ, 156, 123
Astropy Collaboration, Robitaille, T. P., Tollerud, E. J., et al. 2013, A&A, 558, A33
Banzatti, A., Salyk, C., Pontoppidan, K. M., et al. 2025, AJ, 169, 165
Bewketu Belete, A., Andreani, P., Fernández-Ontiveros, J. A., et al. 2021, A&A, 654, A24
Black, J. H., & van Dishoeck, E. F. 1987, ApJ, 322, 412
Boersma, C., Bauschlicher, C. W., Allamandola, L. J., et al. 2010, A&A, 511, A32
Böker, T., Beck, T. L., Birkmann, S. M., et al. 2023, PASP, 135, 038001
Brum, C., Diniz, M. R., Riffel, R. A., et al. 2019, MNRAS, 486, 691
Cazzoli, S., Arribas, S., Maiolino, R., & Colina, L. 2016, A&A, 590, A125
Cicone, C., Maiolino, R., Sturm, E., et al. 2014, A&A, 562, A21
Contini, M., & Viegas, S. M. 1991, A&A, 251, 27
Contini, M., Viegas, S. M., & Prieto, M. A. 2004, MNRAS, 348, 1065
Costa-Souza, J. H., Riffel, R. A., Souza-Oliveira, G. L., et al. 2024, ApJ, 974, 127
Crenshaw, D. M., & Kraemer, S. B. 2012, ApJ, 753, 75
Crenshaw, D. M., Kraemer, S. B., Gabel, J. R., et al. 2004, ApJ, 612, 152
Crenshaw, D. M., Schmitt, H. R., Kraemer, S. B., Mushotzky, R. F., & Dunn, J. P. 2009, ApJ, 708, 419
Dabrowski, I. 1984, CaJPh, 62, 1639
Dall'Agnol de Oliveira, B., Storchi-Bergmann, T., Morganti, R., Riffel, R. A., & Ramakrishnan, V. 2023, MNRAS, 522, 3753
Dasyra, K. M., & Combes, F. 2011, A&A, 533, L10
Dasyra, K. M., Paraschos, G. F., Combes, F., et al. 2024, ApJ, 977, 156
Davies, R. I., Sternberg, A., Lehnert, M. D., & Tacconi-Garman, L. E. 2005, ApJ, 633, 105
Davies, R. L., Belli, S., Park, M., et al. 2024, MNRAS, 528, 4976
Delaney, D. E., Hicks, E. K. S., Zhang, L., et al. 2025, ApJ, 993, 217
den Brok, M., Seth, A. C., Barth, A. J., et al. 2015, ApJ, 809, 101
Dors, O. L., Jr., Riffel, R. A., Cardaci, M. V., et al. 2012, MNRAS, 422, 252
Draine, B. T., & Woods, D. T. 1990, ApJ, 363, 464
Emonts, B. H. C., Colina, L., Piqueras-López, J., et al. 2017, A&A, 607, A116
Emonts, B. H. C., Piqueras-López, J., Colina, L., et al. 2014, A&A, 572, A40
Escott, E. L., Morabito, L. K., Scholtz, J., et al. 2025, MNRAS, 536, 1166
Fabian, A. C. 2012, ARA&A, 50, 455
Ferguson, J. W., Korista, K. T., & Ferland, G. J. 1997, ApJS, 110, 287
Fielding, D. B., & Bryan, G. L. 2022, ApJ, 924, 82
Filippenko, A. V., & Ho, L. C. 2003, ApJL, 588, L13
Fiore, F., Feruglio, C., Shankar, F., et al. 2017, A&A, 601, A143
Fischer, T. C., Crenshaw, D. M., Kraemer, S. B., & Schmitt, H. R. 2013, ApJS, 209, 1
Fluetsch, A., Maiolino, R., Carniani, S., et al. 2019, MNRAS, 483, 4586
Fonseca-Faria, M. A., Rodríguez-Ardila, A., Contini, M., Dahmer-Hahn, L. G., & Morganti, R. 2023, MNRAS, 524, 143
Freitas, I. C., Riffel, R. A., Storchi-Bergmann, T., et al. 2018, MNRAS, 476, 2760
García-Bernete, I., Ramos Almeida, C., Landt, H., et al. 2017, MNRAS, 469, 110
García-Bernete, I., Rigopoulou, D., Donnan, F. R., et al. 2024, A&A, 691, A162
Gatto, L., Storchi-Bergmann, T., Riffel, R. A., et al. 2024, MNRAS, 530, 3059
Goold, K., Seth, A., Molina, M., et al. 2026, arXiv:2601.16977
Gordon, K. D., Clayton, G. C., Decleir, M., et al. 2023, ApJ, 950, 86
Greene, J. E., Setton, D., Bezanson, R., et al. 2020, ApJL, 899, L9
Greenfield, P., & Miller, T. 2016, A&C, 16, 41
Harris, C. R., Millman, K. J., van der Walt, S. J., et al. 2020, Natur, 585, 357
Harrison, C. M., Alexander, D. M., Mullaney, J. R., & Swinbank, A. M. 2014, MNRAS, 441, 3306
Harrison, C. M., Costa, T., Tadhunter, C. N., et al. 2018, NatAs, 2, 198
Hatziminaoglou, E., Hernán-Caballero, A., Feltre, A., & Piñol Ferrer, N. 2015, ApJ, 803, 110
Hermosa Muñoz, L., Alonso-Herrero, A., Pereira-Santaella, M., et al. 2024, A&A, 690, A350
Hill, M. J., & Zakamska, N. L. 2014, MNRAS, 439, 2701
Hunter, J. D. 2007, CSE, 9, 90
Inami, H., Armus, L., Charmandaris, V., et al. 2013, ApJ, 777, 156
Izumi, T., Wada, K., Imanishi, M., et al. 2023, Sci, 382, 554
Jakobsen, P., Ferruit, P., Alves de Oliveira, C., et al. 2022, A&A, 661, A80
Jones, O. C., Álvarez-Márquez, J., Sloan, G. C., et al. 2023, MNRAS, 523, 2519
Kaufman, M. J., Wolfire, M. G., & Hollenbach, D. J. 2006, ApJ, 644, 283
King, A., & Pounds, K. 2015, ARA&A, 53, 115
Koo, B.-C., Raymond, J. C., & Kim, H.-J. 2016, JKAS, 49, 109
Kristensen, L. E., Godard, B., Guillard, P., Gusdorf, A., & Pineau des Forêts, G. 2023, A&A, 675, A86
Krug, H. B., Rupke, D. S. N., & Veilleux, S. 2010, ApJ, 708, 1145
Kwan, J. H., Gatley, I., Merrill, K. M., Probst, R., & Weintraub, D. A. 1977, ApJ, 216, 713
Labiano, A., Argyriou, I., Álvarez-Márquez, J., et al. 2021, A&A, 656, A57
Laha, S., Reynolds, C. S., Reeves, J., et al. 2021, NatAs, 5, 13
Lambrides, E. L., Petric, A. O., Tchernyshyov, K., Zakamska, N. L., & Watts, D. J. 2019, MNRAS, 487, 1823
Lambrides, E. L., Petric, A. O., Tchernyshyov, K., Zakamska, N. L., & Watts, D. J. 2019, MNRAS, 487, 1823
Law, D. R., E. Morrison, J., Argyriou, I., et al. 2023, AJ, 166, 45
Leftley, J. H., Nesvadba, N. P. H., Bicknell, G. V., et al. 2024, A&A, 689, A314
Luridiana, V., Morisset, C., & Shaw, R. A. 2015, A&A, 573, A42
Maccagni, F. M., Santoro, F., Morganti, R., et al. 2016, A&A, 588, A46

Maloney, P. R., Hollenbach, D. J., & Tielens, A. G. G. M. 1996, ApJ, 466, 561
Marconcini, C., Feltre, A., Lamperti, I., et al. 2025, A&A, 701, A113
Mizumoto, M., Nomura, M., Done, C., Ohsuga, K., & Odaka, H. 2021, MNRAS, 503, 1442
Mizumoto, M., Sameshima, H., Kobayashi, N., et al. 2024, ApJ, 960, 41
Mor, R., Netzer, H., & Elitzur, M. 2009, ApJ, 705, 298
Morganti, R., & Oosterloo, T. 2018, A&ARv, 26, 4
Mouri, H. 1994, ApJ, 427, 777
Müller-Sánchez, F., Prieto, M. A., Hicks, E. K. S., et al. 2011, ApJ, 739, 69
Nandi, P., Stalin, C. S., Dam, P., & Saikia, D. J. 2024, ApJ, 973, 7
Nandi, P., Stalin, C. S., & Saikia, D. J. 2025, ApJ, 984, 20
Nandi, P., Stalin, C. S., Saikia, D. J., et al. 2023a, ApJ, 950, 81
Nandi, P., & Subramonian Stalin, C. 2024, BSRSL, 93, 780
Nandi, P., Stalin, C. S., Saikia, D. J., et al. 2023b, ApJ, 959, 116
Narayanan, D., Krumholz, M. R., Ostriker, E. C., & Hernquist, L. 2012, MNRAS, 421, 3127
Ogle, P., Boulanger, F., Guillard, P., et al. 2010, ApJ, 724, 1193
Oliva, E., Marconi, A., Maiolino, R., et al. 2001, A&A, 369, L5
Osterbrock, D. E., & Ferland, G. J. 2006, Astrophysics of Gaseous Nebulae and Active Galactic Nuclei (2nd ed.; Univ. Science Books)
Pandey, S., Rakshit, S., Chand, K., et al. 2024, ApJ, 976, 116
Parlanti, E., Carniani, S., Venturi, G., et al. 2025, A&A, 695, A6
Penny, S. J., Masters, K. L., Smethurst, R., et al. 2018, MNRAS, 476, 979
Pereira-Santaella, M., Diamond-Stanic, A. M., Alonso-Herrero, A., & Rieke, G. H. 2010, ApJ, 725, 2270
Pereira-Santaella, M., Colina, L., García-Burillo, S., et al. 2018, A&A, 616, A171
Pereira-Santaella, M., Colina, L., García-Burillo, S., et al. 2020, A&A, 643, A89
Pereira-Santaella, M., Álvarez-Márquez, J., García-Bernete, I., et al. 2022, A&A, 665, L11
Pereira-Santaella, M., García-Bernete, I., González-Alfonso, E., et al. 2024, A&A, 685, L13
Perrin, M. D., Sivaramakrishnan, A., Lajoie, C.-P., et al. 2014, SPIE, 9143, 91433X
Perrin, M. D., Soummer, R., Elliott, E. M., Lallo, M. D., & Sivaramakrishnan, A. 2012, SPIE, 8442, 84423D
Peterson, B. M., Bentz, M. C., Desroches, L.-B., et al. 2005, ApJ, 632, 799
Pontoppidan, K. M., Salyk, C., Banzatti, A., et al. 2024, ApJ, 963, 158
Pound, M. W., & Wolfire, M. G. 2008, AAS, 394, 654
Pound, M. W., & Wolfire, M. G. 2011, PDRT: Photo Dissociation Region Toolbox, Astrophysics Source Code Library, ascl:1102.022
Pound, M. W., & Wolfire, M. G. 2023, AJ, 165, 25
Reines, A. E., & Volonteri, M. 2015, ApJ, 813, 82
Revalski, M., Crenshaw, D. M., Rafelski, M., et al. 2022, ApJ, 930, 14
Richings, A. J., & Faucher-Giguère, C.-A. 2018, MNRAS, 478, 3100
Rieke, G. H., Wright, G. S., Böker, T., et al. 2015, PASP, 127, 584
Riffel, R. A. 2021, MNRAS, 506, 2950
Riffel, R. A., Souza-Oliveira, G. L., Costa-Souza, J. H., et al. 2025, ApJ, 982, 69
Riffel, R. A., Storchi-Bergmann, T., Zakamska, N. L., & Riffel, R. 2020, MNRAS, 496, 4857
Riffel, R. A., Dors, O. L., Armah, M., et al. 2021, MNRAS, 501, L54
Riffel, R. A., Storchi-Bergmann, T., Riffel, R., et al. 2023, MNRAS, 521, 1832
Rigopoulou, D., Donnan, F. R., García-Bernete, I., et al. 2024, MNRAS, 532, 1598
Rodríguez-Ardila, A., & Cerqueira-Campos, F. 2025, FrASS, 12, 1548632
Rodríguez-Ardila, A., Fonseca-Faria, M. A., Dahmer-Hahn, L. G., et al. 2025, MNRAS, 538, 2800
Rodríguez-Ardila, A., Pastoriza, M. G., Viegas, S., Sigut, T. A. A., & Pradhan, A. K. 2004, A&A, 425, 457
Rodríguez-Ardila, A., Riffel, R., & Pastoriza, M. G. 2005, MNRAS, 364, 1041
Rodríguez-Ardila, A., Viegas, S. M., Pastoriza, M. G., & Prato, L. 2002, ApJ, 579, 214
Rupke, D. S. N., Thomas, A. D., & Dopita, M. A. 2021, MNRAS, 503, 4748
Rupke, D. S. N., & Veilleux, S. 2013, ApJ, 768, 75
Ruschel-Dutra, D., Storchi-Bergmann, T., Schnorr-Müller, A., et al. 2021, MNRAS, 507, 74
Salvestrini, F., Gruppioni, C., Hatziminaoglou, E., et al. 2022, A&A, 663, A28
Sandstrom, K. M., Chastenet, J., Sutter, J., et al. 2023, ApJL, 944, L7
Smith, J. D. T., Draine, B. T., Dale, D. A., et al. 2007, ApJ, 656, 770
Smith, M. D. 1995, A&A, 296, 789
Sternberg, A. 1989a, ApJ, 347, 863
Sternberg, A. 1989b, in Proc. 22nd Eslab Symp., Infrared Spectroscopy in Astronomy, ed. E. Böhm-Vitense (ESA), 269
Sternberg, A., & Dalgarno, A. 1989, ApJ, 338, 197
Storchi-Bergmann, T., McGregor, P. J., Riffel, R. A., et al. 2009, MNRAS, 394, 1148
Su, R., Mahony, E. K., Gu, M., et al. 2023, MNRAS, 520, 5712
Sutherland, R. S., & Dopita, M. A. 2017, ApJS, 229, 34
Tappe, A., Rho, J., & Reach, W. T. 2006, ApJ, 653, 267
Thim, F., Hoessel, J. G., Saha, A., et al. 2004, AJ, 127, 2322
Tombesi, F., Cappi, M., Reeves, J. N., et al. 2010, A&A, 521, A57
Tommasin, S., Spinoglio, L., Malkan, M. A., et al. 2008, ApJ, 676, 836
Veilleux, S., Maiolino, R., Bolatto, A. D., & Aalto, S. 2020, A&ARv, 28, 2
Virtanen, P., Gommers, R., Oliphant, T. E., et al. 2020, NatMe, 17, 261
Wright, G. S., Wright, D., Goodson, G. B., et al. 2015, PASP, 127, 595
Wright, G. S., Rieke, G. H., Glasse, A., et al. 2023, PASP, 135, 048003
Zhang, L., Packham, C., Hicks, E. K. S., et al. 2024, ApJ, 974, 195